Exploring ice sheet model sensitivity to ocean thermal forcing and basal sliding using the Community Ice Sheet Model (CISM)

Mira Berdahl[1,3], Gunter Leguy[2], William H. Lipscomb[2], Nathan M. Urban[3,4], and Matthew J. Hoffman[3]

[1]Department of Earth and Space Sciences, University of Washington, WA, USA
[2]Climate and Global Dynamics Laboratory, National Center for Atmospheric Research, Boulder, CO, USA
[3]T-3 Group, Los Alamos National Laboratory, Los Alamos, NM, USA
[4]Computational Science Initiative, Brookhaven National Laboratory, Upton, NY, USA

Correspondence: Mira Berdahl (mberdahl@uw.edu)

Abstract. Multi-meter sea level rise (SLR) is thought to be possible within **[the next few centuries]**, with most of the uncertainty originating from the Antarctic land ice contribution. One source of uncertainty relates to the ice sheet model initialization. Since ice sheets have a long response time (compared to other Earth system components such as the atmosphere), ice sheet model initialization methods can have significant impacts on how the ice sheet responds to future forcings. To assess this, we generated 25 different ice sheet spin-ups, using the Community Ice Sheet Model (CISM) at 4km resolution. During each spin-up we varied two key parameters known to impact the sensitivity of the ice sheet to future forcing: one related to the sensitivity of the ice-shelf melt rate to ocean thermal forcing, and the other related to the basal friction. The spin-ups all nudge toward observed thickness and enforce a no-advance calving criterion, such that all final spun-up states resemble observations but differ in their melt and friction parameter settings. Each spin-up was then forced with future ocean thermal forcings from 13 different CMIP6 models under the SSP5-8.5 emissions scenario, and modern climatological surface mass balance data. Our results show that the effects of the ice sheet and ocean parameter settings used during the spin-up are capable of impacting multi-century future SLR predictions by as much as 2 m. By the end of this century, the effects of these choices are more modest, but still significant, with differences of up to 0.2 m of SLR. We have identified a combined ocean and ice parameter space that leads to widespread mass loss **[within 500 years]** (low friction & high melt rate sensitivity). To explore temperature thresholds, we also ran a synthetically-forced CISM ensemble that is focused on the Amundsen region only. Given certain ocean and ice parameter choices, Amundsen mass loss can be triggered with thermal forcing anomalies between 1.5 and 2°C **[relative to the spin-up]**. Our results emphasize the critical importance of considering ice sheet/ocean parameter choices during spin-up for sea level rise predictions **[and suggest the importance of including glacial isostatic adjustment in ice sheet simulations]**.

1 Introduction

The Antarctic ice sheet **[(AIS)]** has the potential to contribute multiple meters to global mean sea level (GMSL) **[on timescales of several centuries]**. Yet, Antarctic contributions to sea level rise (SLR) remain the largest source of uncertainty in future projections, particularly on the multi-century timescale (Pattyn and Morlighem, 2020). This is largely due to inadequate model

resolution and process representation (Berdahl et al., 2021) and climate uncertainty (Edwards et al., 2021; Seroussi et al., 2020).

25   Recent projections from the Ice Sheet Model Comparison Project for CMIP6 (ISMIP6) suggest SLR contributions ranging from -7.8 to 30 cm after 100 years under the Representative Concentration Pathway (RCP) 8.5 scenario – spanning the possibilities of either net continental mass loss or growth (Seroussi et al., 2020). Part of this large range is due to **[poorly known processes]** in glaciological dynamics (ie. no consensus on what processes to include or how to include them) (Berdahl et al., 2021; Kopp et al., 2017; Bakker et al., 2017). **[One study that included novel physics (eg. hydrofracture and cliff failure leading to**

30   **Marine Ice Cliff Instability (MICI))]** projected much higher 21st century SLR contributions of more than 1 m (DeConto and Pollard, 2016). Recent discussions by Edwards et al. (2021) and DeConto et al. (2021) highlight the continued debate not only regarding the degree of contribution to sea level from Antarctica over the coming centuries, but also the mechanisms that contribute to mass loss.

   Despite these open questions, it remains well-known that the Antarctic Ice Sheet has been losing mass for at least the past

35   four decades, with most of the melt concentrated in the Amundsen and Bellingshausen Seas in West Antarctica (Rignot et al., 2019). This is largely due to a radiative/wind-driven increase in delivery of relatively warm Circumpolar Deep Water (CDW) to the marine-based ice shelves in the West Antarctic Ice Sheet (WAIS) (Rignot et al., 2013; Holland et al., 2019). As the warmer water thins the shelves, the buttressing back-stress they provide to upstream flow is reduced, leading to increased grounded-ice discharge and a subsequent increase in SLR (Fürst et al., 2016; Gudmundsson et al., 2019). Due to a reversing bed slope under

40   much of the WAIS, it is particularly susceptible to positive feedbacks in mass loss. It has been suggested that this process, called the Marine Ice Sheet Instability (MISI), (Weertman, 1974; Schoof, 2007), has already been triggered at glaciers such as the Thwaites and Pine Island Glaciers (Joughin et al., 2014; Favier et al., 2014).

   Despite large advances in ice sheet modeling (Pattyn, 2018), the sensitivity of the WAIS to changing climate and its influence on local ocean conditions are challenging for models. One major unknown is the thermal forcing (TF) in the ice shelf cavity

45   itself, which is rarely explicitly resolved in current Atmosphere-Ocean Global Climate Models (AOGCMs). Furthermore, understanding how ocean TF translates to melt rates at the grounding line is still an open question – the functional relationship between TF and melt rates remains speculative. It is therefore a vital question both how forcing will change and how sensitive the Antarctic Ice Sheet is to such forcings.

   Borne from the need to systematically quantify the uncertainties in sea level rise from Antarctica, a number of ice sheet model

50   intercomparison projects have been organized. The notion that initialization methods can impact ice sheet simulations is well-known and was explored with 16 different ice sheet models under the initial state intercomparison project (initMIP) framework (Seroussi et al., 2019). ISMIP6 is the most extensive ice sheet model intercomparison project to date (Seroussi et al., 2020). Detailed in Nowicki et al. (2020), 13 ice sheet modeling groups performed a suite of standardized and open experiments aimed at exploring the relative roles of climate forcings, climate warming scenarios, sub-shelf melt parameterizations, multi-model

55   forcing and ice sheet model spread in SLR from Antarctica. ISMIP6 was tasked with generating ocean boundary conditions for stand-alone ice sheet models underneath ice shelves (unresolved in the AOGCMs). To do this, ocean variables were extrapolated horizontally from continental shelves into the ice shelf cavities. Then a melt rate parameterization was used to convert ocean TF to melt rates (more details in Section 1.1). In general, all of the proposed melt rate schemes are trying to account for complex

ocean processes (i.e., translating far-field ocean characteristics to sub-shelf melt rates) with simple equations. However, many parameters used in these approximations are not well constrained, and there remains no scientific consensus on the optimal functional form of basal melt parameterizations. Indeed, Seroussi et al. (2020) concluded that sensitivity to melt rates was one of the largest sources of uncertainty in future projections of the AIS.

In their extended ISMIP6 study, Lipscomb et al. (2021) found two parameters to be especially important to the sensitivity of the ice sheet. The first, γ_0, is a constant in the TF parameterization that scales melt rates for a given ocean TF. This parameter **[controls]** the strength of ice shelf melt to ocean warming and cannot be uniquely calibrated from observations due to the need for a poorly constrained TF bias correction term. Preliminary efforts using these parameterizations have focused on capturing the range of these effects by sampling high/moderate/low values for γ_0 (e.g. Jourdain et al. (2020); Lipscomb et al. (2021); Nowicki et al. (2020)). In their emulation study, Edwards et al. (2021) found that γ_0 was a similar magnitude, or larger, contributor to uncertainty in their projections of sea level rise as global warming under a particular emissions scenario. The second parameter, p, affects the effective pressure near the grounding line, and is specific to how CISM handles **[basal]** friction. **[p represents the proportion of marine based ice supported by sea water pressure.]** It essentially dictates the degree of basal slipperiness, particularly in marine-based ice. Both γ_0 and p are set during the model spin-up (more detail in Section 2) and play a role in the conditioning of the ice sheet. As a result, a new ice sheet spin-up must be run for each combination of p and γ_0 in future runs. A large range of p and γ_0 combinations can yield acceptable spun up states that have different **[sensitivities to future ocean warming]**. **[In other words, the choices of p and γ_0 during the spin-up affect the resulting basal friction field and sub-shelf conditions, which in turn affect the ice sheet's sensitivity to ocean thermal forcing.]** Therefore, any future simulations of the ice sheet strongly hinge on what spin-up settings were used because they dictate how strongly the ice sheet will respond to a forcing. Indeed, it is possible that these parameters may be more important to mass loss projections than the future forcing itself.

In this study, we expand the scope of the previous initMIP and ISMIP6 studies by running a 25-member spin-up ensemble of an ice sheet model, designed to probe the sensitivity of the ice sheet to γ_0 and p in greater detail. The intent is for our spin-ups to reach steady state with thickness being close to today's observations. Therefore, each spun-up ice sheet state resembles a modern AIS configuration (ie. all spun-up states are valid in this regard, yet non-unique in the p and γ_0 parameters). Each spin-up member is then forced with future ocean conditions from 13 different CMIP6 models. This allows us to test how future forcings manifest under different ice sheet sensitivities that occur simply by virtue of these two parameter choices. We also perform synthetically-forced future runs in just the Amundsen region in order to more systematically assess the sensitivity of this critical region to both p and γ_0. In the next section, we describe in more detail how γ_0 and p fit into the mathematical framework of our ice sheet simulations.

1.1 Two important parameters: p and γ_0

In this section we summarize the sub-shelf melt rate parameterizations used in the ISMIP6 framework. More details can be found in Jourdain et al. (2020). There are two main versions of the basal melt parameterization, known as *local* and *non-local*. The *local* parameterization assumes that the sub-shelf melt-induced circulation develops locally to reinforce turbulence and

subsequent melting, and represents the influence of ocean stratification. The *non-local* version parameterizes melt rate as the product of the local TF and the nonlocal TF (ie. sector-average TF). This is rooted in the idea that the melt rate is proportional to both the local TF and the cavity-scale circulation (Holland et al., 2008).

Constant	Value	Description/Units
ρ_i	918.0	Ice density (kg/m^3)
ρ_{sw}	1028.0	Sea water density (kg/m^3)
L_f	3.34×10^5	[~~Ice density~~ Latent heat of fusion] (kg/m^3)
c_{pw}	3974.0	Specific heat of sea water ($Jkg^{-1}K^{-1}$)

Table 1. Physical constants used in the quadratic melt parameterizations.

Both the local and non-local versions have two options for calibration, known as *MeanAnt* (Mean Antarctica) and *PIGL* (Pine Island Grounding Line). Parameters are calibrated at the scale of 16 regional sectors. The most basic form (*local*), not shown here, computes basal melt rates beneath ice shelves as a quadratic function of their forcing, with a TF correction suggested by Jourdain et al. (2020). The melt rate parameterization most commonly used in ISMIP6 is the *non-local* version, which takes the quadratic form:

$$m(x,y) = \gamma_0 \times \left(\frac{\rho_{sw}c_{pw}}{\rho_i L_f} \right)^2 \times (TF(x,y,z_{draft}) + \delta T_{sector}) \times |\langle TF \rangle_{draft \epsilon sector} + \delta T_{sector}| \qquad (1)$$

where z_{draft} is the ice shelf thickness below the waterline, $TF(x,y,z_{draft})$ is the TF at the ice-ocean interface and $\langle TF \rangle_{draft \epsilon sector}$ is the TF averaged over all the ice-shelves of an entire sector. δT_{sector} is a temperature correction for a regional sector used as a means to reproduce observation-based melt rates from observation-based TF, and has a maximum negative value of -2°C. In other words, δT_{sector} is used to correct for biases in sparse ocean observations, biases in climate model ocean temperature and salinity, and in the melt parameterization itself. γ_0 is an empirical uniform coefficient with units of velocity. The constants, ρ_i (density of ice), ρ_{sw} (density of sea water), c_{pw} (specific heat of seawater), and L_f (ice density) are given in Table 1.

There is also a non-local, slope-dependent quadratic melting parameterization of the form used in Lipscomb et al. (2021)

$$m(x,y) = \gamma_0 \times \left(\frac{\rho_{sw}c_{pw}}{\rho_i L_f} \right)^2 \times (TF(x,y,z_{draft}) + \delta T_{sector}) \times |\langle TF \rangle_{draft \epsilon sector} + \delta T_{sector}| \times \sin(\theta) \qquad (2)$$

where θ is the local angle between the ice-shelf base and the horizontal. **[The slope can change as the geometry evolves in the simulation.]** The slope dependence is included based on theoretical arguments by Jenkins (2016) and Little et al. (2009), suggesting that basal slope controls the entrainment of heat, therefore affecting melt rates. Jenkins (2016) shows that the basal slope plays a role in driving Ekman pumping and suction analogous to that of the wind stress curl in classical ocean circulation theory. Typically, the steeper the basal slope, the stronger the Ekman pumping.

Jourdain et al. (2020) generated a distribution of possible γ_0 values in order to reproduce either the observed present-day Antarctic melt rates (averaged over a sector), *MeanAnt* calibration, or the (much higher) *PIGL* calibration melt rates. ISMIP6 participants then sampled low (5th percentile), medium (median) and high (95th percentile) γ_0 values as a nominal exploration

of the sensitivity of ice sheet projections to γ_0. Values of γ_0 for the **[non-local]** and non-local slope parameterizations are shown in Table 2.

Parameterization	Calibration	5th percentile γ_0 (m/s)	Median γ_0 (m/s)	95th percentile γ_0 (m/s)
Non-local	MeanAnt	9.62×10^3	1.44×10^4	2.10×10^4
Non-local	PIGL	8.80×10^4	1.59×10^5	4.71×10^5
Non-local slope	MeanAnt	1.47×10^6	2.06×10^6	2.84×10^6
Non-local slope	PIGL	2.93×10^6	5.37×10^6	2.94×10^7

Table 2. Calibrated γ_0 (m/s) values calculated for the non-local parameterizations in the ISMIP6 protocol in Jourdain et al. (2020) and Lipscomb et al. (2021).

120   To focus computing resources and analysis on one scheme, we choose to limit this study to the slope-dependent non-local form (Eq. 2), since, **[at the time the ensemble was run, it was believed to be the most realistic scheme [(Jenkins et al., 2018)]]**. Since we are testing sensitivity to γ_0, we are not using a specific calibrated parameter range. The simulations in our paper differ from the ISMIP6 protocols in the treatment of δT_{sector}. Instead of using the values suggested by Jourdain et al. (2020) to match observational estimates of basal melting in each sector, we tune δT_{sector} to obtain melt rates that drive the ice

125   toward the observed ice thickness near the grounding line, as described by Lipscomb et al. (2021). In some basins, this results in basin-average melt rates that differ appreciably from observational estimates. For more details, see Section 3.1 of Lipscomb et al. (2021).

In addition to finding that γ_0 had a large impact on sea level projections, Lipscomb et al. (2021) found that mass loss from the ice sheet was strongly dependent on the degree of water-pressure support from the ocean. We use a basal sliding law based

130   on Schoof (2005) (Eq. 6) in which the effective pressure exhibits a smooth transition from a finite value to zero at the grounding line. This is given by the following expression (suggested by Asay-Davis et al. (2016)) describing the basal shear stress, τ_b :

$$\tau_b = \frac{C_p C_c N}{[C_p^m |u_b| + (C_c N)^m]^{\frac{1}{m}}} |u_b|^{\frac{1}{m}-1} u_b, \tag{3}$$

where C_p is an empirical coefficient for power-law behavior, C_c is an empirical coefficient for Coulomb behavior **[(set to 0.5 as in Asay-Davis et al. (2016) and Lipscomb et al. (2021))]**, u_b is the basal ice velocity, N is the effective pressure, and $m = 3$

135   is a power law exponent. **[(We acknowledge that the choice of C_c can affect the results. This is addressed in Sec. 4.)]**

Following Leguy et al. (2014), a simple function for the effective pressure that accounts for connectivity between the subglacial drainage system and the ocean is given by

$$N(p) = \rho_i g H \left(1 - \frac{H_f}{H}\right)^p, \tag{4}$$

where g is gravitational acceleration, $H_f = max(0, -\frac{\rho_{sw}}{\rho_i}b)$ is the flotation thickness and b is the bed elevation, defined as

140   negative below sea level. The parameter p varies from zero (no basal water pressure) to one (the subglacial drainage system is hydrologically well connected to the ocean and there is full support near the grounding line). When $p = 0.5$, there is partial

support of the ice overburden by subglacial water pressure. **[This parameterization only accounts for basal sliding for ice grounded below sea level. It does not account for subglacial hydrology in regions where the glacier bed is above sea level. A hydrology model for CISM is currently in development.]** In the interior of the ice sheet, and when $p = 0$, this law asymptotes to power-law behavior:

$$\tau_b \approx C_p |u_b|^{\frac{1}{m}-1} u_b. \tag{5}$$

In the grounding line zone, when $p > 0$, the bed provides little resistance to sliding, and the basal shear stress approaches Coulomb friction behavior:

$$\tau_b \approx C_c N \frac{u_b}{|u_b|}. \tag{6}$$

Importantly, under Coulomb behavior, the ice becomes more sensitive to the loss of ice-shelf buttressing (Sun et al., 2020).

Lipscomb et al. (2021) tested the impacts of choosing $p = 0$, $p = 0.5$ and $p = 1$ on sea level contributions. They found differences of up to $\sim$500 mm in sea level contributions by 2500 compared to runs using a power-law shear stress formulation, concluding that weaker basal friction makes the ice more vulnerable to melt. In this study, we expand on this work by more extensively sampling across p (25 values instead of two) in order to better understand the potential impacts on ice mass loss. **[We note that while γ_0 is forcing-related and therefore transferable across ice sheet models, p is a model-internal parameter and might not be directly transferable. Our formulation with p applies to sliding laws in which basal friction depends on the effective pressure N. Other models with similar sliding laws can therefore benefit from this study.]**

2 Methods

2.1 Community Ice Sheet Model: Configuration & Spin-up Methodology

We use the Community Ice Sheet Model (CISM), a state-of-the-art 3D, parallel, thermo-mechanical model that runs on a regular mesh grid (Lipscomb et al., 2019). CISM has participated in various ice sheet model intercomparisons (e.g. MISMIP+ (Cornford et al., 2020), LARMIP (Levermann et al., 2020), ABUMIP **[(Sun et al., 2020)]**, initMIP (Seroussi et al., 2019) and ISMIP6 (Nowicki et al., 2020; Seroussi et al., 2020)), and its output was comparable to other higher-order ice sheet models, some of which use resolutions of 1 km or higher in the region containing the grounding line.

[For continental-scale simulations, ice sheet models are typically run at resolutions of 4 km or coarser (Seroussi et al., 2019). On century timescales, Lipscomb et al. (2021) found CISM was only moderately sensitive to grid resolution in ocean-forced AIS experiments, concluding that 4 km resolution was comparable to 2 km resolution. Leguy et al. (2021) found that CISM grid resolutions of 2-4 km may be sufficient to represent grounding line migration. Therefore, all continental-scale, Antarctic simulations were run on a uniform 4 km grid] and used the following options:

- A depth-integrated higher-order solver based on Goldberg (2011).

- A basal sliding law based on Schoof (2005).

- Grounding line parameterizations for basal shear stress and basal melt rate (Leguy et al., 2014, 2021). Basal melting is applied to partially floating cells in proportion to the floating fraction of the cell, which is diagnosed from the thickness and bed topography.

175   - **[A no-advance calving criterion that holds the calving front near its observed location. During forward runs, the calving front is allowed to change location as the ice melts, and it can re-advance, but cannot advance past its original observed location.]**

- Geothermal heat flux from Shapiro and Ritzwoller (2004).

The original spin-up, taken from Lipscomb et al. (2021), is run with the nonlocal-slope parameterization and $\gamma_0 = 2.06 \times$
180   $10^6 \mathrm{m\ yr^{-1}}$ (Table 2). The spin-up method, described in Lipscomb et al. (2021), adjusts a 2D basal friction parameter field (C_p) beneath grounded ice and δT_{sector} under floating ice in order to match observed ice sheet properties with little drift. The ice sheet is initialized to the present-day thickness using the BedMachineAntarctica data set (Morlighem et al., 2020). The surface mass balance (SMB) is from a late 20th century simulation with the RACMO2.3 regional climate model (van Wessem et al., 2018). SMB is held constant using the RACMO2 1976-2016 climatology in the spin-up and forward runs.
185   [~~There is no hydrology in the basal friction field.~~] The basal melt rates are computed directly from the TF **[climatological data set spanning 1995-2018 from Jourdain et al. (2020)]**, [~~using the climatological data set~~] and the non-local slope parameterization [~~,~~] described in Section 1.1. As the model is nudged toward observations, the ice thickness gradually evolves to a quasi-steady state. The result is a spun-up state with good agreement between observed and modeled surface velocity (Fig. 1), ice shelf extent, and ice thickness (Fig. 2), except in regions that are known to be out of steady state, such as the
190   Amundsen sector and the Kamb Ice Stream **[(seen in Fig. 1)]**.

While this initialization procedure works well to keep grounded ice near observed thicknesses and removes low-frequency oscillations associated with slow changes in basal temperature, the sensitivity of the ice sheet is highly impacted by the choice of parameters during forward runs. This study was devised as a way to address this concern directly. Here, we investigate how two key parameters (p and γ_0) that condition the ice during spin-up affect sea level contributions under future forcing scenarios.

195   ## 2.2   Spin-up ensemble design

In order to explore the effect of p and γ_0 on the ice sheet sensitivity, a new spin-up must be run for each combination of parameters. We ran a 25-member spin-up ensemble with p and γ_0 values shown in Table 3. We used a stratified Latin hypercube sampling technique (McKay et al., 1979) from a non-uniform distribution of p and γ_0. Figure 3 shows the sampling distributions for p and γ_0. From basic physical arguments, p is constrained to be in the range $[0, 1]$. Previous experimental results (Lipscomb
200   et al., 2021) revealed that the differences in SLR on multi-century timescales between $p = 0$ and $p = 0.5$ are smaller than the differences in SLR between $p = 0.5$ and 1.0 **[and are mainly driven by ocean forcing rather than the value of p (see Figure A1 for additional details)]**. This suggests that the space could be explored more efficiently by having a greater sampling density for values near 1. That said, there is no *a priori* mechanistic argument for one end of the range being more
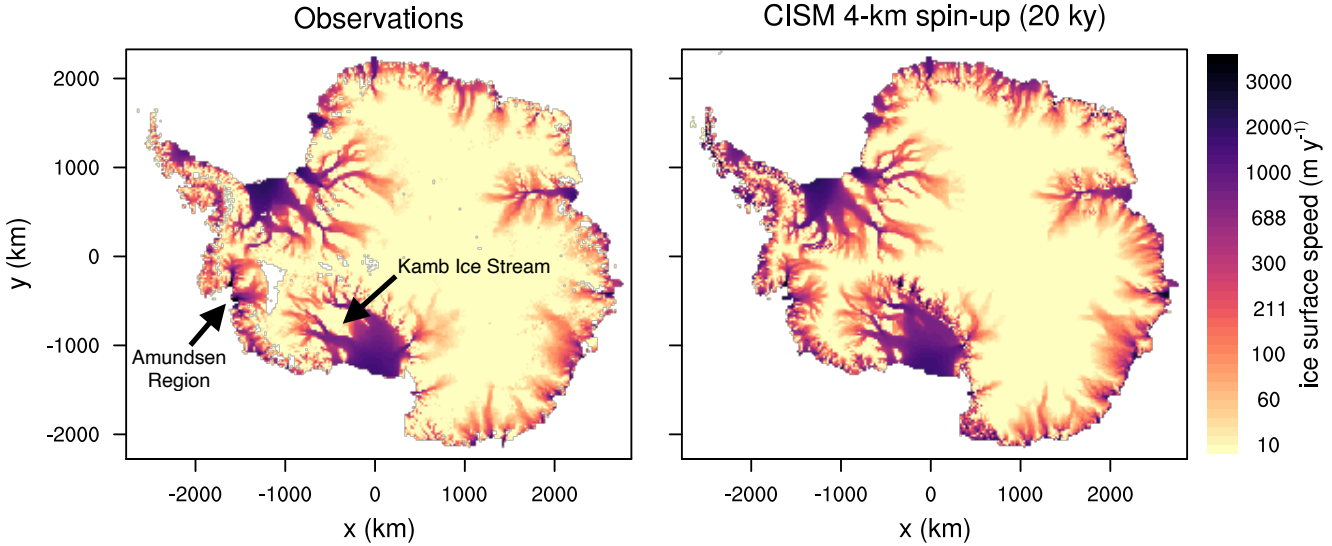
Figure 1. [Observed (left panel) (Rignot et al., 2011) and modeled (right panel) Antarctic surface speed (m/yr, log scale) for the initial spun-up state used to initialize our 25 ensemble spin-ups (using $p = 0$ and $\gamma_0 = 2062539$). The root-mean-square error between observed and modeled velocity is 128.7 m/yr. White patches represent missing data.]
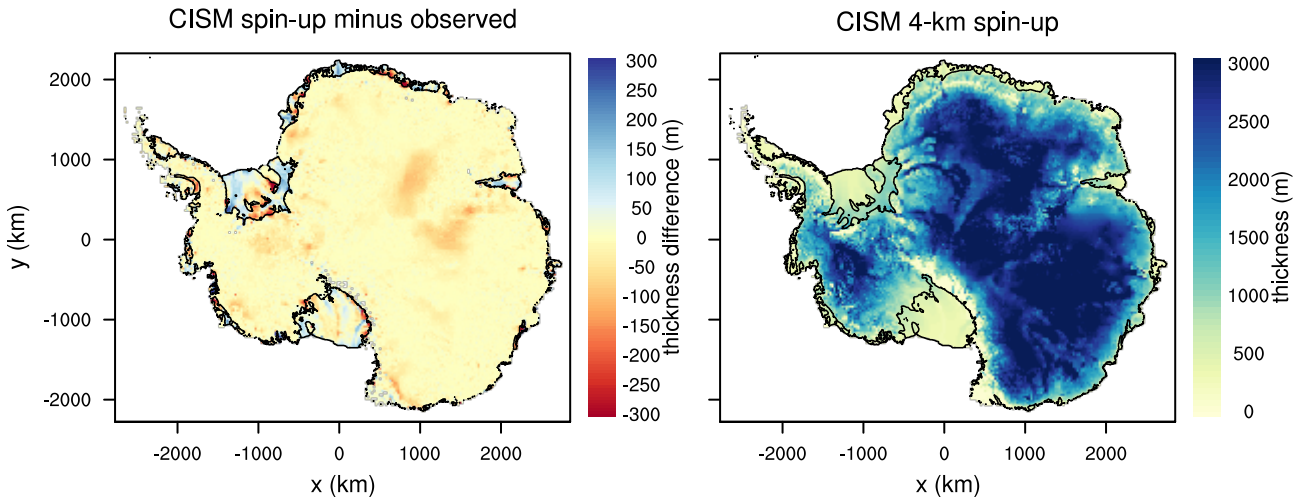
Figure 2. Difference between modeled and observed ice thickness (left) and modeled ice thickness (right) [for the initial spin-up state used to initialize our 25 ensemble spin-ups (using $p = 0$ and $\gamma_0 = 2062539$), with root-mean-square error 51.8 m]. Observations are from the BedMachine Antarctica data set (Morlighem et al., 2020).

physically correct than the other. We chose a truncated power distribution, with weighting heavier toward $p = 1$. Specifically,
205 $\pi(p) = (\alpha + 1)p^\alpha$, bounded on $[0, 1]$ with $\alpha = 1.5$ (Figure 3, y-axis).

Suggested ISMIP6 calibrated median γ_0 values for the non-local parameterizations are shown in Table 2. The γ_0 value is closely tied to the physical assumptions. With slope dependence, γ_0 needs to be about 100 times larger. We develop a distribution of γ_0 that spans both the $MeanAnt$ and $PIGL$ ranges. We used the distribution $\pi(\gamma_0) \propto \frac{1}{(a\gamma_0-1)^2+1}$, bounded on $[1.47 \times 10^6, 1.0 \times 10^7]$. We chose $a = 3.5 \times 10^{-7}$ such that values would fall preferentially within the MeanAnt range rather than the high end of the PIGL range (Figure 3, x-axis). Note that the upper value is truncated to be 10^7 instead of $\sim 3 \times 10^7$ as experimentation suggests that the latter value is far too high (N. Jourdain, personal communication, Nov 12, 2020).
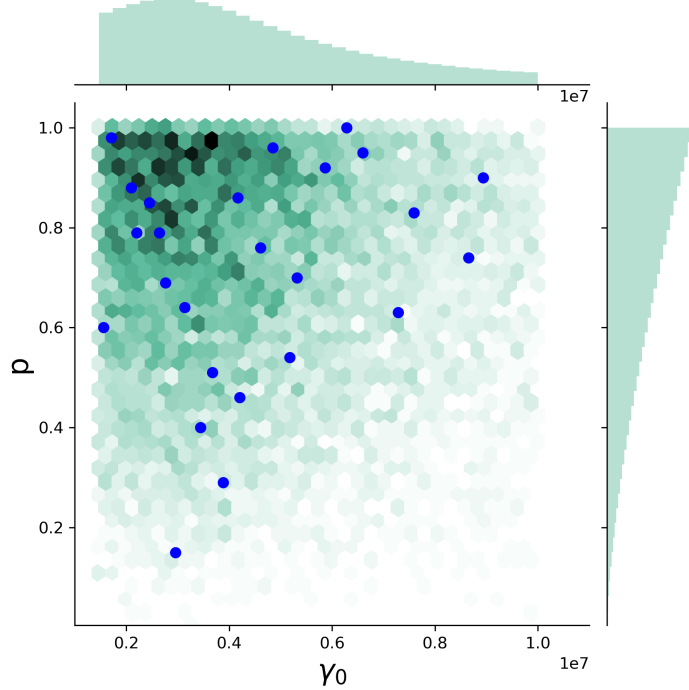
Figure 3. Joint sampling distribution for p and γ_0 used for sampling the spin-up ensemble values (green), and actual chosen p and γ_0 combinations for this ensemble, using a stratified Latin hypercube sampling from a non-uniform distribution of p and γ_0 (blue dots).

Each spin-up is branched from the original spin-up in Lipscomb et al. (2021) (Sec. 2.1) and run for at least 10,000 years further. To ensure the spin-up is in steady-state, **[the mass change rate must not exceed** $1\,\mathrm{Gt yr^{-1}}$ **]. [Also, the floating ice area for the continent and just the Amundsen Sea sector must not exceed a 1% change per year.]** Figure 4 shows ice sheet metrics (ice mass, grounded ice mass, grounded ice area and grounding line flux) for each spin-up ensemble member, as well as current observational estimates. Spin-ups all converge toward similar states, and the total and grounded ice mass and grounded ice area are close to observed (BedMachine Antarctica V2, (Morlighem et al., 2020)) values. **[As noted earlier, the RACMO2 historical SMB climatology is used, with spin-up SMB $\sim$2500 Gt/yr compared to observed $\sim$2300 Gt/yr (Mottram et al., 2021; Rignot et al., 2019)). Observational estimates of basal mass balance (BMB) are $\sim$1300 Gt/yr (Rignot et al., 2013; Depoorter et al., 2013), while typical spin-up values are about 630 Gt/yr. This discrepancy between**

Ensemble Member	p	γ_0 (m/s)	$\delta T_{Amundsen}$ (°C)	Ensemble Member	p	γ_0 (m/s)	$\delta T_{Amundsen}$ (°C)
1	0.15	2954923	-1.6	14	0.79	2200776	-2
2	0.29	3886395	-1.79	15	0.79	2640377	-2
3	0.4	3440211	-1.8	16	0.83	7593133	-2
4	0.46	4205230	-1.98	17	0.85	2450186	-2
5	0.51	3677928	-2	18	0.86	4167483	-2
6	0.54	5175963	-2	19	0.88	2098892	-2
7	0.6	1560081	-1.98	20	0.9	8939808	-2
8	0.63	7280916	-2	21	0.92	5864477	-2
9	0.64	3139194	-2	22	0.95	6598244	-2
10	0.69	2760685	-2	23	0.96	4849305	-2
11	0.7	5321878	-2	24	0.98	1710386	-2
12	0.74	8654548	-2	25	1.0	6285577	-2
13	0.76	4609682	-2				

Table 3. [p and γ_0 combinations for each ensemble member, along with the $\delta T_{Amundsen}$, showing the end of spin-up correction factor needed for this region.]

observed and modeled BMB is in large part due to the large $\delta T_{Amundsen}$ values, discussed in greater detail below. Spun-up calving fluxes are around 2000 Gt/yr, while observed values are roughly 1300 Gt/yr (Depoorter et al., 2013). Since the spun-up BMB is reduced from present-day values as a result of ocean cooling, the calving fluxes must make up the difference, which results in spun-up calving fluxes larger than observed.]

225   Here we choose to prioritize initializing the ice sheet to be close to equilibrium at the expense of a perfect match to the observed ice mass state. For the purposes of this work, we consider the end-of-spinup state to be representative of an ice sheet under 'current' conditions, in that thicknesses are close to today's ice sheet. Therefore, forward runs that begin with forcing at 1995-2005 levels are applied directly to the spun-up ice sheet state. The end-of-spinup $\delta T_{Amundsen}$ values for each new parameter setting are given in Table 3. **[Figure 5 shows the ensemble mean and standard deviation end-of-spinup**
230   **thickness, velocity, and δT values for all regions.]**

    [The assumption of an ice sheet at equilibrium is unrealistic, especially for the Amundsen sector. The large negative values in Table 3 reflect this assumption. They show that in order to match the ice sheet's current configuration during spin-up, a large negative thermal correction was necessary to cool the ocean to prevent retreat. To overcome the artificially cooled ocean temperatures in the Amundsen, we also run a set of synthetic experiments targeting only the
235   **Amundsen region (further details in 2.4). More discussion on the TF correction factors in Table 3, specifically what they imply with respect to our assumption about a 'current' state, can be found in Section 3.]**
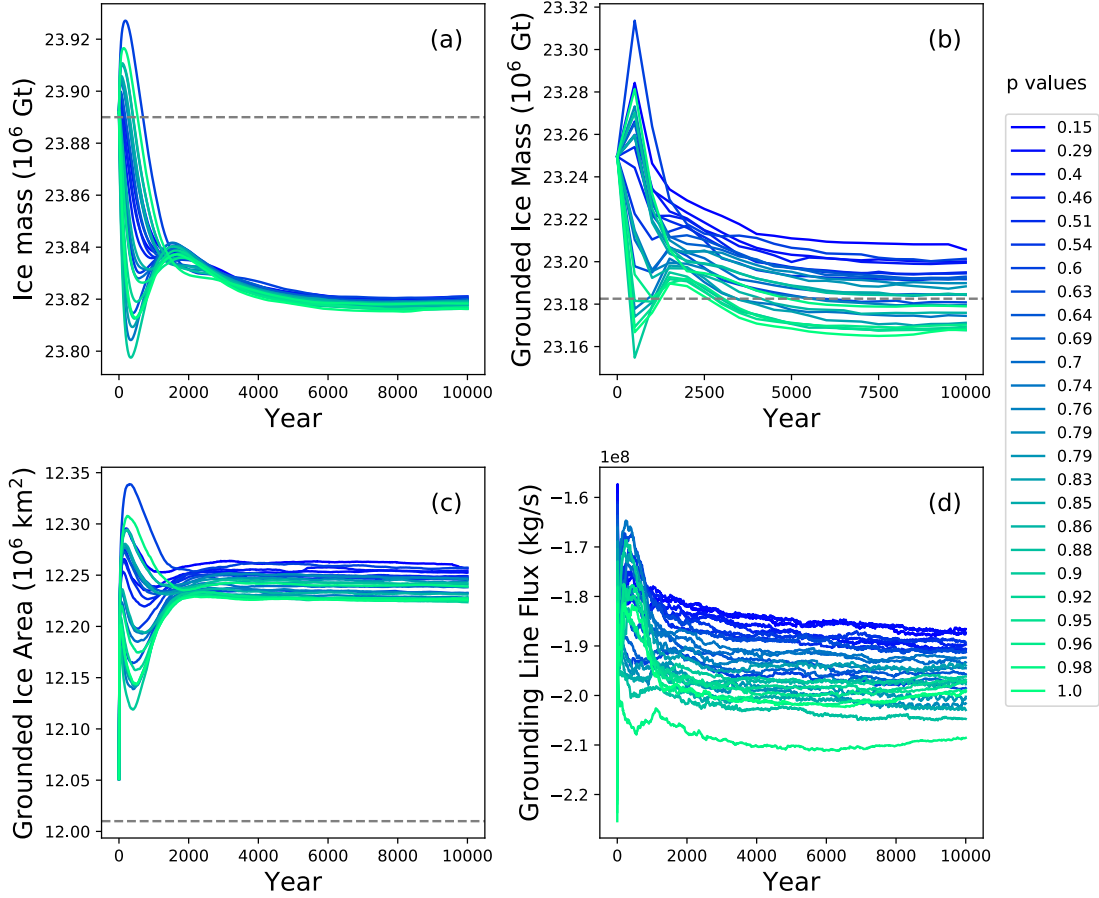
Figure 4. Time series for ice mass (a), grounded ice mass (b), grounded ice area (c) and grounding line flux (d) for the 25 spin-up ensemble members. Legend indicates the value of p for each ensemble member. Grey dashed lines indicate observational estimates, as calculated from the BedMachine Antarctica V2 dataset (Morlighem et al., 2020). **[Note that the frequency of model output is sparser in panel (b) because it was derived using variables with less frequent output.]**

2.3 Forward simulations: CMIP6 SSP58.5

To assess the effect of p and γ_0 on the sensitivity of the ice sheet in a multi-model framework, forward simulations were forced using AOGCM-derived ocean conditions. Since both of these parameters relate to ice shelf behavior, and in order to focus on the effects of ocean forcing in the forward runs, SMB is held constant at historical values. TF was computed from 13 CMIP6 climate models and applied as anomalies to each spun-up ice sheet state. Specifically, 3D fields of temperature, salinity and density were extracted from 13 CMIP6 climate models for the high emissions SSP8.5 scenario (Table 4) for two decadally-averaged time slices: 1995-2005 and 2090-2100. These were then area-averaged according to the Linear Antarctic Response to basal melting – Model Intercomparison Project (LARMIP) basins (Levermann et al., 2020): Antarctic Peninsula (AP), Weddell
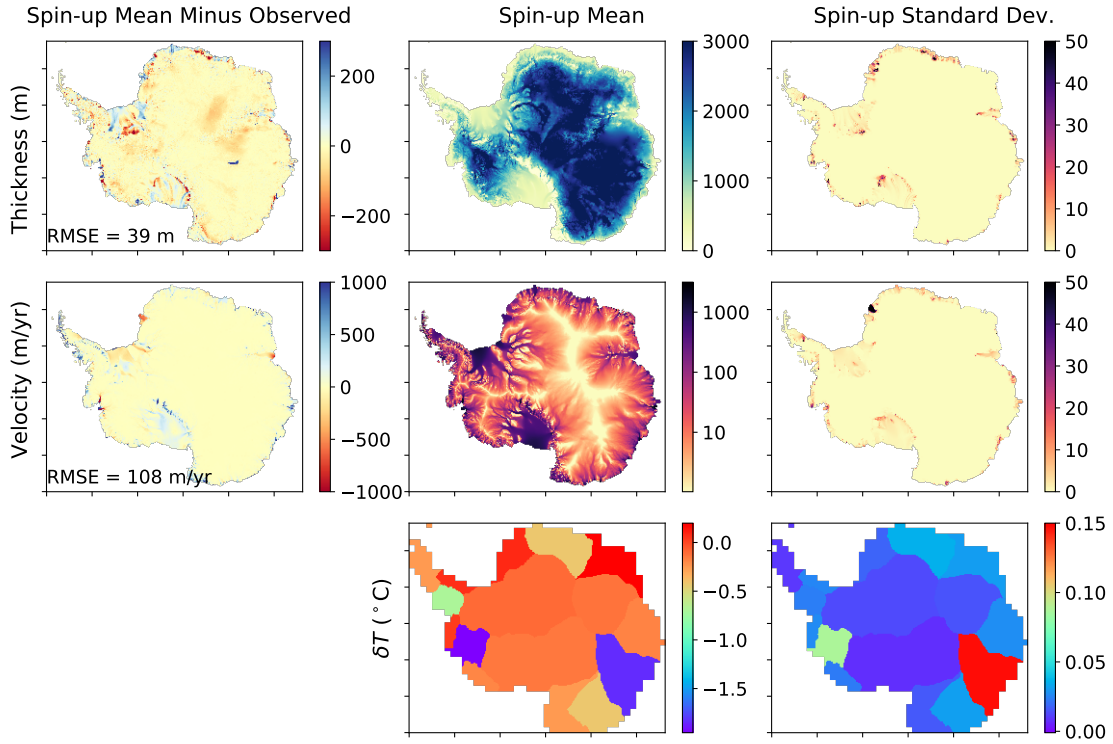
Figure 5. [End-of-spinup statistics: Thickness (top row), surface velocity (center row) and δT values (bottom row). Columns show the end-of-spinup mean minus observed values (left column), spin-up mean (center column) and standard deviation (STD) (right column). Spin-up mean and STD are computed across all 25 p and γ_0 ensemble members. Observed thickness is from the BedMachine Antarctica V2 (Morlighem et al., 2020), and observed velocities are from Mouginot et al. (2014).]

245 **[(aka Filchner–Ronne)]**, Amundsen, Ross, and East Antarctic (Fig 6) and interpolated onto the CISM grid (30 depth layers from 0 to 1800 m at 60 m intervals). The TF was then computed by taking the difference between the *in situ* ocean temperature and the *in situ* freezing temperature.

CISM reads the midpoint of the depth grid. The TF at the lower ice surface is then linearly interpolated between the two adjacent TF values. In the case that the ice draft is located above the top level or below the bottom level, the nearest TF value

250 is used. In forward runs, CISM is forced with a TF anomaly. Therefore, we subtracted the 1995–2005 mean TF profile from the 2090-2100 mean TF profile which gave our 2090–2100 TF anomaly profile. CISM anomalies in the future runs begin with zero anomaly at all depths, and monotonically **[change]** at each depth level to the final 2090-2100 TF anomaly profile, shown in Figure 7.

CMIP6 Model Name	Country	Atmos. Resolution (lon x lat)	Ocean Resolution (horizontal)	Ocean Vertical Levels	Key Reference
BCC-CSM2-MR	China	$1.9° \times 1.3°$	$1° \times 1°$	40	Wu et al. (2019)
CAMS-CSM1-0	China	$1.1° \times 1.1°$	$1° \times 1°$	50	Xin-Yao et al. (2019)
CESM2	USA	$1.3° \times 0.9°$	$1° \times 1°$	60	Danabasoglu et al. (2020)
CNRM-CM6-1	France	$1.4° \times 1.4°$	$1° \times 1°$	75	Voldoire et al. (2019)
CNRM-ESM2-1	France	$1.4° \times 1.4°$	$1° \times 1°$	75	Séférian et al. (2019)
CanESM5	Canada	$2.8° \times 2.8°$	$1° \times 1°$	45	Swart et al. (2019)
EC-Earth3	Europe	$0.7° \times 0.7°$	$1° \times 1°$	75	Döscher et al. (2021)
EC-Earth3-Veg	Europe	$0.7° \times 0.7°$	$1° \times 1°$	75	Wyser et al. (2020)
GFDL-CM4	USA	$1° \times 1°$	$0.25° \times 0.25°$	75	Held et al. (2019)
GFDL-ESM4	USA	$1.3° \times 1°$	$0.5° \times 0.5°$	75	Dunne et al. (2020)
IPSL-CM6A-LR	France	$2.5° \times 1.3°$	$1° \times 1°$	75	Lurton et al. (2020)
MPI-ESM1-2-HR	Germany	$0.9° \times 0.9°$	$0.4° \times 0.4°$	40	Müller et al. (2018)
NESM3	China	$1.9° \times 1.9°$	$1° \times 1°$	46	Cao et al. (2018)

Table 4. Names, resolutions and references for the CMIP6 models used in this study.

Thus, each spun-up CISM state (25 p and γ_0 ensemble members) is branched into 13 forward runs, all forced by CMIP6-derived TFs under the SSP5-8.5 scenario. The forward runs are extended for another 400 years using constant 2090–2100 mean forcing profile, such that the full effects of end-of-century forcings are realized.

2.4 Forward simulations: Synthetic perturbations in the Amundsen Sea Sector

The glaciers in the Amundsen region have lost more mass than any other sector over the past several decades (Paolo et al., 2015), yet the thresholds and projections of future loss are still not well constrained (Nias et al., 2019). Therefore, in addition to the CMIP6-forced ensemble, we ran a set of synthetically-forced CISM runs, where TF anomalies are applied only in the Amundsen Region in order to explore parameter and forcing settings that lead to Thwaites mass loss or collapse. We ran forward simulations with a maximum TF anomaly of 1°C, 1.5°C and 2°C, applied uniformly with depth to the Amundsen region only, while the other regions are kept at zero TF anomaly for the duration of the run. The Amundsen anomaly is ramped up linearly starting from zero in the 1995–2005 period to the maximum value of the experiment (1°C, 1.5°C and 2°C) at the 2090–2100 mean. This final maximum forcing is then extended, remaining constant for another 400 years. These synthetic forcings are applied to the same spin-up ensemble used in the CMIP6 SSP5-8.5 experiments.

As discussed in Section 1.1, δT_{sector} is a temperature correction, with units of temperature, for a regional sector used to reproduce observation-based melt rates from observation-based TF. It is important to note the final $\delta T_{Amundsen}$ values in Table 3 in the context of these synthetic TF experiments. The $\delta T_{Amundsen}$ corrections are consistently negative with values
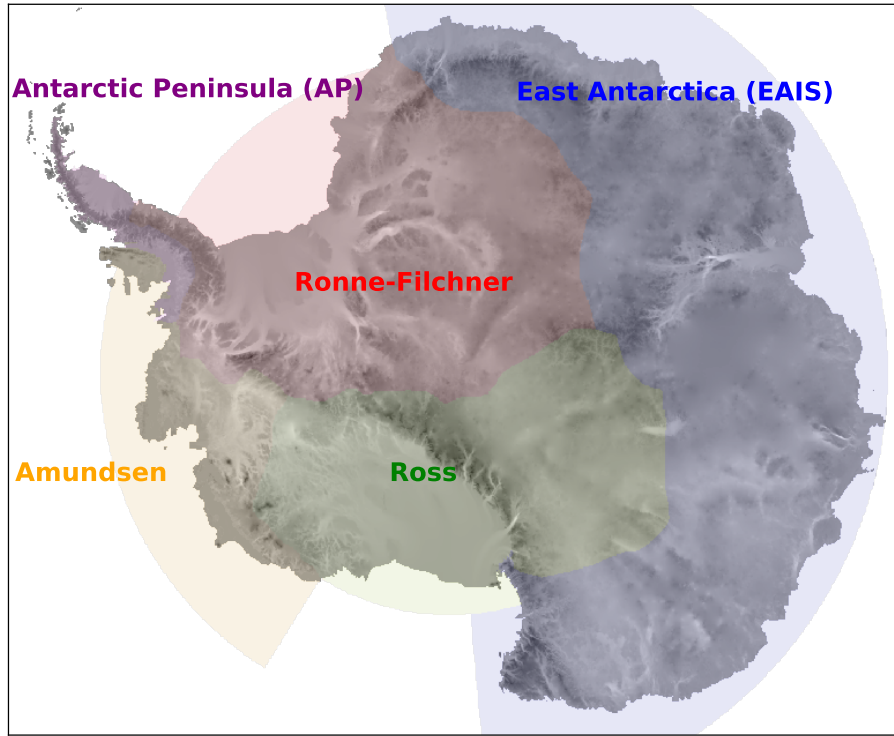
Figure 6. Map of basins used in this study, based on the LARMIP delineations Levermann et al. (2020).

270   ranging from -1.6°C to -2°C. This means that significant cooling is needed to slow grounding-line retreat that occurs under climatological TF during the spin-up. Therefore, the spun-up melt rates in the Amundsen are lower than observed. Negative values of δT_{sector} may also be compensating for other errors such as biases in climatology or the misplacement of ocean heat. Lipscomb et al. (2021) posit that another possibility for such large temperature corrections in the Amundsen Sea is that the TF derived from the 1995–2018 climatology used in their spin-up exceeds the forcing that was typical in the mid 20th century and

275   before. In this case, negative δT_{sector} would be correcting for the recent warming, to generate melt rates closer to pre-industrial values. Therefore, in forward runs we would need a relatively large TF anomaly (∼2°C) to raise melt rates to observed present-day values. **[In that sense, the Amundsen anomaly experiments can also be viewed as estimates of committed SLR under warming that has already occurred.]** Thus, we consider our synthetic experiments ranging from 1-2°C TF anomaly to be physically sensible.
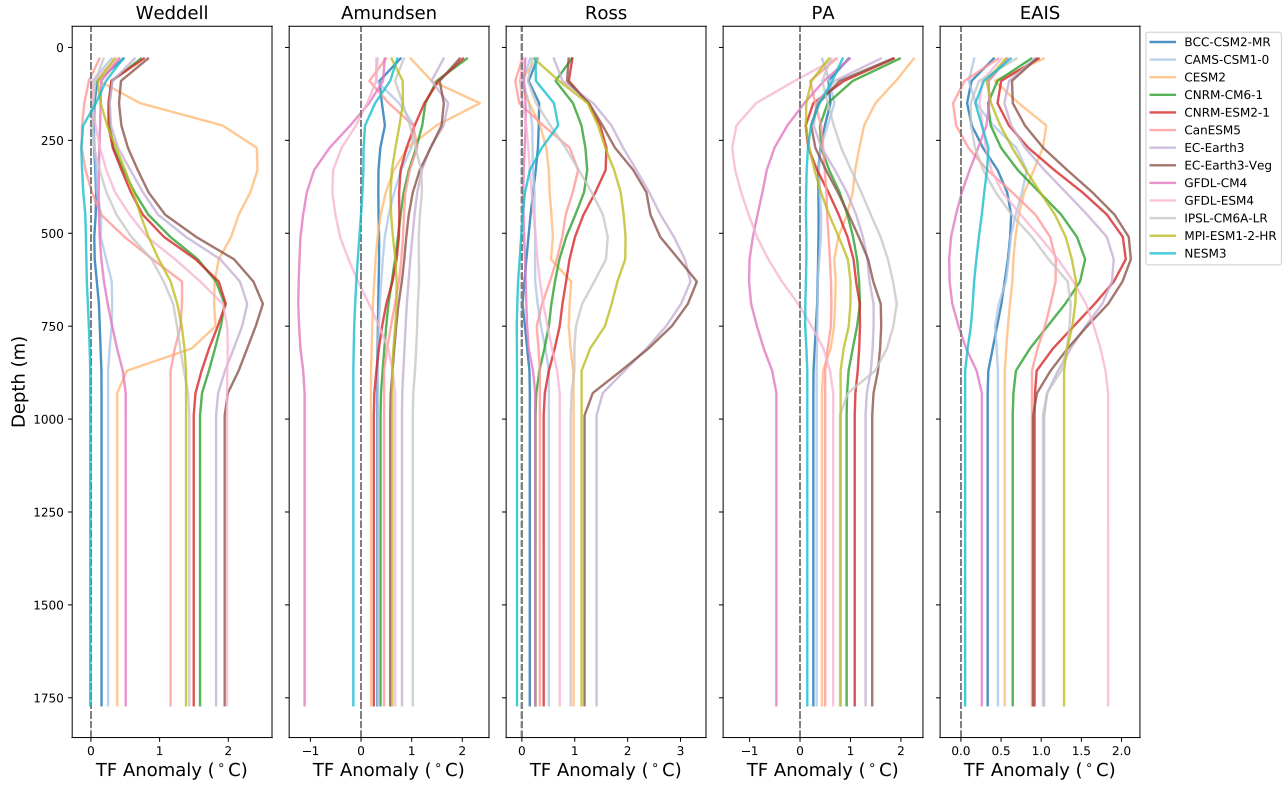
Figure 7. Final thermal forcing (TF) anomaly profile for each basin. The TF anomaly begins at zero at all ocean levels. The anomaly grows linearly at each level until it reaches the mean 2090-2100 anomaly. After this, the 2090-2100 mean value is held constant for another 400 years.

3 Results of Forward Experiments

3.1 CMIP6 TF simulations

3.1.1 Continental Results

Given that the distributions of p and γ_0 were non-uniform by design, our ensemble does not have a physically meaningful prior (e.g., the distribution on p was intentionally chosen to over-sample the more sensitive values of p, possibly favoring high SLR more than physically warranted). Therefore, the results presented below such as the predicted ranges of SLR should not be over-interpreted. Similarly, the summary statistics shown in Figure A3 are presented to describe the qualitative behavior of the sea level rise.

The CMIP6-forced forward experiments result in a wide range of final sea level after 500 years, depending on the parameter and forcing combinations used (Table A1, Figure 8). The final SLR across all parameters and model forcings ranges between

290   2 mm and 300 mm after 100 years, and 47.5 mm and 3.17 m after 500 years. Critically, the combined choice of p and γ_0 alone has the potential to generate large differences in final SLR contributions. Examining the absolute range of final SLR for a given forcing, the choice of p and γ_0 causes anywhere from a modest difference of 70 mm (NESM3) to a large difference of almost 2 m (EC-Earth3-Veg, (Table A1 **[and Fig. A2)]**). For any given CMIP6 forcing, the choice of p and γ_0 produces a 2–3 fold change between the highest and lowest final SLR value. The choice of p and γ_0 has a more limited, but still significant impact

295   on SLR after 100 years. The largest difference in SLR after 100 years for a given model is 215 mm (EC-Earth3-Veg), and the smallest is 3.1 mm (NESM3). Therefore, the impacts of the choice of p and γ_0 during spin-up could mean the difference between basin-wide ice collapse or not on multi-century timescales. Even though the differences are less pronounced **[at year 100 than year 500, they still constitute critical impacts on end-of-century sea level estimates.]** The difference of 0.2 m for the EC-Earth3-Veg forced run, for example, has is highly relevant to societal decision making for low-lying coastal regions. It

300   is worth noting that since the spin-up method can produce a steady state with a delayed response to warming, the differences seen after 100 years may be underestimated. The ensemble spread of SLR for all ensemble members (p and γ_0 combinations) after 100 and 500 years of simulation are further illustrated in Figure 8. The models with the smallest spread and lowest SLR (BCC-CSM2-MR, CAMS-CSM1-0, GFDL-CM4 and NESM3) are also those with the weakest forcing, particularly at ∼250–700 m depth (approximate depths of grounding lines) in the largest regions (Weddell, EAIS and Ross) (Figure 7). The

305   EC-Earth3 models generate the strongest forcing at the grounding line depths, and therefore produce the highest SLR in the Weddell, Ross and EAIS sectors.

    In general, the EC-Earth3-Veg model produces the largest SLR after 500 years, while the NESM3 model produces the least SLR (Figure A3(a)).The slope of the curves in the log-log plot (Figure A3(b)) indicates the scaling of SLR. Across all models there is little to no change initially in sea level because the forcing is still minimal as it begins to ramp up. This is followed by

310   an abrupt change to a **[nonlinear]** increase in sea level for about the first 100 years, concurrent with a linear ramp-up of TF. Then, after 100 years, when the forcing becomes constant and is no longer ramping up, the sea-level increase becomes roughly linear. **[Therefore, the rate of change of sea level rise tracks the rate of change of the forcing anomaly being applied (i.e., whether it is increasing or held constant), regardless of the magnitude of forcing.]** This pattern is also illustrated in Figure A3(c), where the SLR rate for the model means shows swift acceleration in the first 100 years of the simulation. This is

315   followed by a steadying in SLR rates once the forcing becomes constant. In the case of the EC-Earth models, the rate of change in Antarctic contributions to sea level reaches ∼4 mm/year after 100 years. This exceeds the current observed rate of global sea level rise of 3.7 mm/year, which includes all global sources over the period 2006-2018 (Fox-Kemper et al., 2021). In other words, these results suggest that under some model forcings, the rate of contribution to sea level from Antarctica (currently modest) could become comparable to the current global rates by the end of the century.

320   The qualitative structure of the final sea level contribution as a function of γ_0 and p is similar across all models, though the magnitudes of mass loss are different across all models (Figure 9). For each model forcing, low γ_0 values produce little sea level rise, while high values produce the most. The final continental sea level contribution in these experiments depends much more on the variation of melt rate with γ_0 than on the change in hydrological connectivity near the grounding line with p. The ensemble mean correlation (R^2) value between final SLR and γ_0 is 0.93, whereas R^2 with p is only 0.15. The linear fits,

325 along with model-specific R^2 value (Figure 10), show the same story across all models: On the continental scale, γ_0 is a much stronger predictor of SLR than is p. [In our experiments, $p > 0.6$ appears to be necessary, but not sufficient, to produce significant sea level rise. This behavior implies that when $p < 0.6$, the effective pressure is large enough to reduce the impact of the applied TF, as opposed to when $p > 0.6$ and the bed has increased hydrological connectivity. High values of p alone are not sufficient to force a strong sea-level response, indicating that the power-law regime dominates in the
330 basal sliding law at the continental scale. However, Joughin et al. (2019) showed that Thwaites and Pine Island Glaciers exhibit Coulomb-sliding behavior, suggesting that a regional analysis is necessary.]
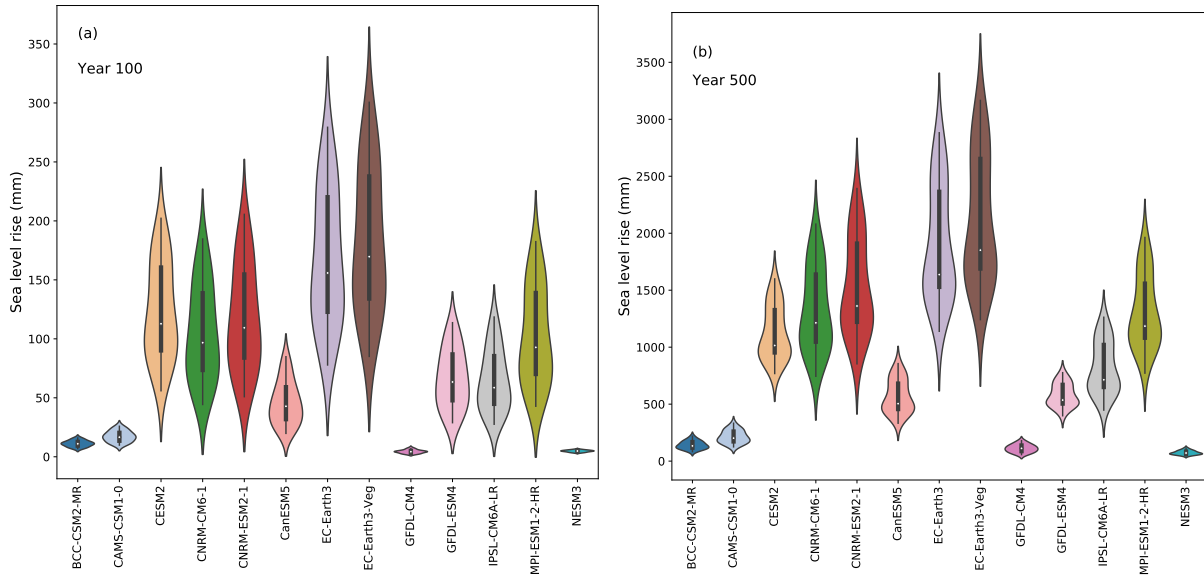
Figure 8. Model spread of SLR after (a) 100 years and (b) 500 years. Note different y-scale in the panels.

3.1.2 Regional Results

When we analyze the SLR by region, we find that most CMIP6-forced runs give a SLR signal dominated by ice loss from the Weddell and Ross regions, and to a lesser extent the EAIS (Figure 11). The regions that contribute least to SLR are the AP
335 and, perhaps surprisingly, the Amundsen. Whereas some models produce strong ocean TF in the Weddell and Ross regions (up to ∼2°C and ∼3°C respectively at GL depths), the maximum forcing in the Amundsen and AP is fairly weak (∼1°C and ∼1.5°C) (Figure 7). This magnitude of forcing in the Amundsen, coupled with the large regional TF corrections (-1.6°C to -2°C, Table 3) generated during spin-up, together result in minimal mass loss. The highest model-mean SLR contribution from the Amundsen region remains below 200 mm.
340 As with the continent-wide assessment, the regional SLR dependence on p and γ_0 appears more strongly controlled by γ_0 than p, particularly when forcing is sufficient to generate large sea level contributions. Specifically, R^2 values describing the correlation strength between sea level contributions and p or γ_0 are shown in Figure 12. There is a consistently strong
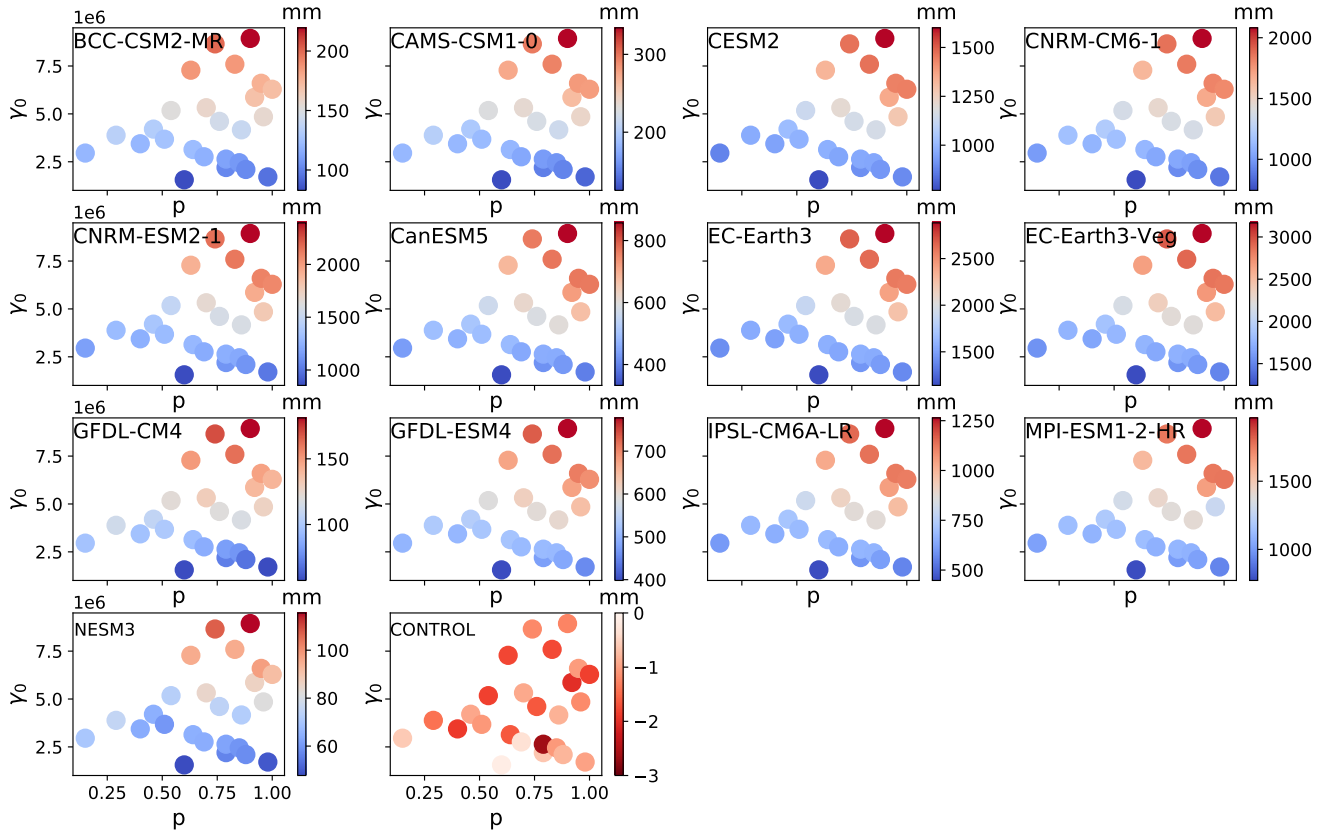
Figure 9. Final SLR for each model, γ_0 and p combination. Note the different colorbar scales for each model.

dependence (high R^2 values) on γ_0 and low dependence on p for the Weddell and Ross regions. These regions are also those that produce the most SLR. The EAIS, though generally generating less SLR, tends to follow the same pattern, with one exception where correlation with γ_0 is low (<0.2). This occurs with a CMIP6 model (GFDL-CM4) which produces little SLR (<20 mm after 500 years) in the region due to weak TF anomalies. Again, the Amundsen and AP show little contribution to SLR, and also tend to have a weaker correlation with γ_0, and in some cases show strong correlation ($R^2 \sim 0.8$) with p. **[In the AP region, the dependence on p is stronger for climate forcing leading to more than 8 mm of SLR (BCC-CSM2-MR, CESM2, CNRM-CM6-1, CNRM-ESM2-1, EC-Earth3, EC-Earth3-Veg).]** Figures A4 to A8 show all final SLR values for each model as a function of p and γ_0, along with their best linear fits.

[As in the continental results, a shift of mass loss melt rates is exhibited at $p \sim 0.6$. For $p < 0.6$, mass loss tends to track p linearly, however for $p > 0.6$, mass loss becomes less dependent on p. Again, this behavior is likely a result of the fact that low p values imply significant effective pressure and less responsive ice. Higher p values allow for a more susceptible grounding zone.]
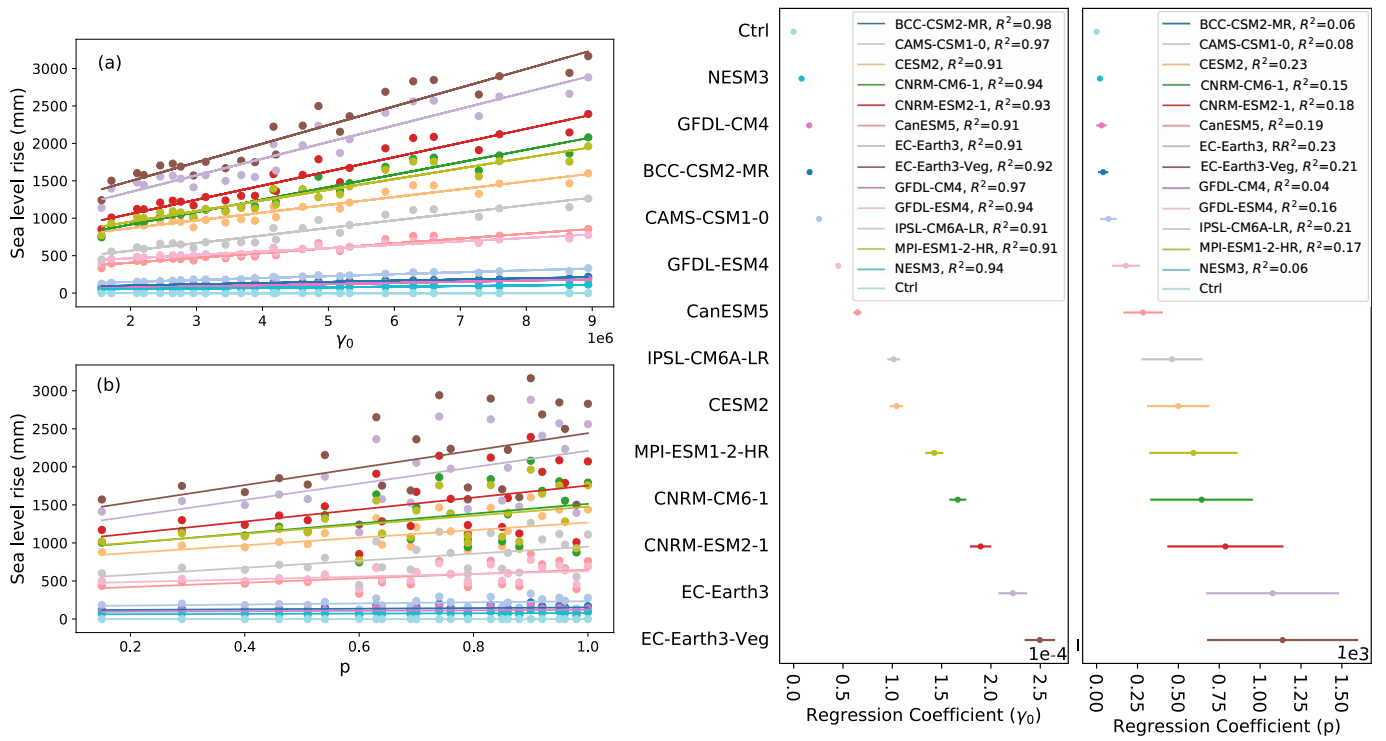
Figure 10. Continental SLR as a function of (a) γ_0 and (b) p with best linear fits. Panels on right show the regression coefficients for the model fits along with their error bars. The R^2 value associated with the best fit line is also shown in the legends.

In the Amundsen region, there appears to be a break-point in final SLR as a function of γ_0 (Figure A5). For $\gamma_0 < 5 \times 10^6$ m/s, sea level remains nearly constant, in some cases rising minimally. For $\gamma_0 > 5 \times 10^6$ m/s, melt rates become large enough that mass loss begins to ramp up as γ_0 increases. In the case of the warmest (EC-Earth) models, close to half a meter of sea level increase is achieved under high γ_0 and high p settings in the Amundsen. With cooler AOGCMs (e.g. GFDL[-CM4], NESM3) the same high p and γ_0 settings are not capable of promoting mass loss. This change in behavior with higher γ_0 in the Amundsen is likely a result of multiple factors. First, the melt rates generated with lower γ_0 values are insufficient to push the ice into deeper retrograde bed-slope regions, and second, the melt rates computed with lower γ_0 values are insufficient to overcome the large negative regional TF corrections resulting from the spinup methodology. Both of these issues will be elaborated in the next section and in Section 4. Further experiments designed to target Amundsen behavior under higher (than CMIP6) forcing are explored in more detail in the following section.
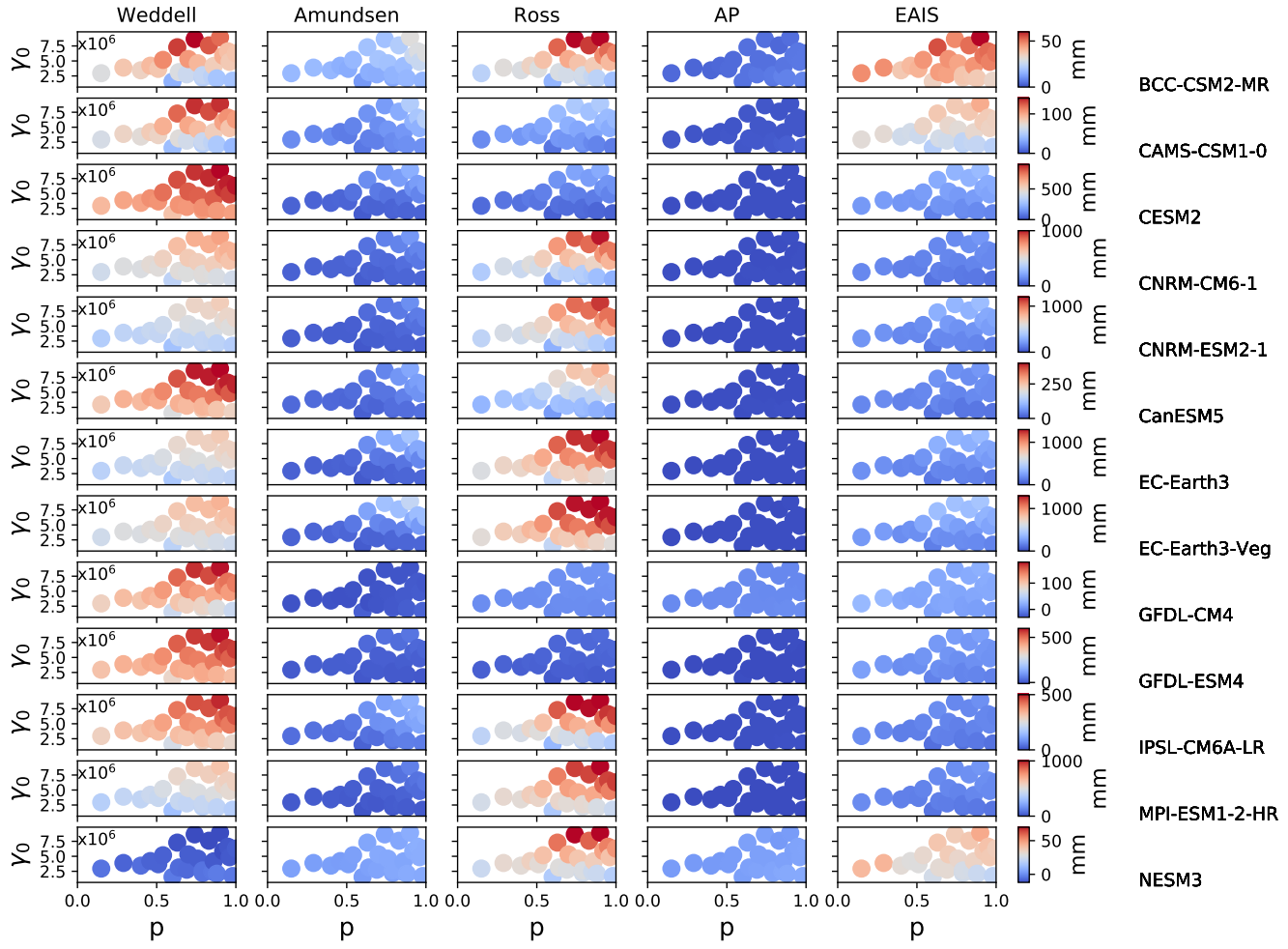
Figure 11. Final (500 year) regional SLR contribution as a function of γ_0 and p. Rows show **[the CMIP6 model used in the forcing. Columns show the region.]** Note the different colorbar scales for each model.

3.2 Synthetic TF perturbations in the Amundsen Sea Sector

We explore the sensitivity of the Amundsen sector using regionally-targeted synthetic TFs. Rapid ice retreat in this region has been observed in the past several decades (Rignot et al., 2019), and it has been suggested that Thwaites Glacier collapse may already be underway (Joughin et al., 2014). The modest response in the Amundsen sector in the CMIP6-forced ensemble can be attributed to the weak forcing in almost all the AOGCMs in this region (Figure 7), along with the large (-1.6°C to -2°C) TF correction. As discussed in Section 2.3 and in Lipscomb et al. (2021)[?], in order for the spin-up to match the ice sheet's current configuration, a large negative thermal correction was necessary to cool the ocean to prevent retreat. However, there is strong evidence that the Amundsen Sea Embayment has recently been warming (Rignot et al., 2019; Jenkins et al., 2018;
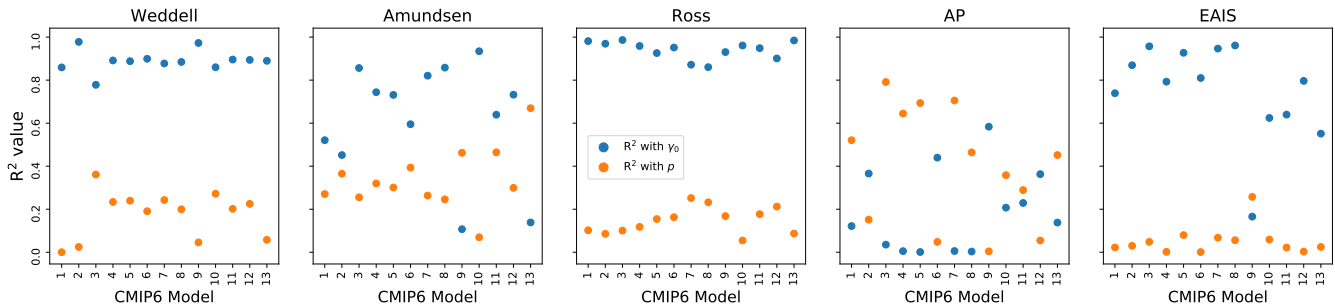
Figure 12. R^2 correlation values for fits between final (year 500) SLR and p (orange) and γ_0 (blue). Panels distinguish region. Each blue/orange regional pair represents one CMIP6 model. The correlations are generally higher with γ_0 than with p, particularly in the Weddell, ross and EAIS regions. In the Amundsen and AP, the TF anomalies are generally weaker and the signal becomes less clear. The corresponding order of CMIP6 model from 1 to 13 is: BCC-CSM2-MR, CAMS-CSM1-0, CESM2, CNRM-CM6-1, CNRM-ESM2-1, CanESM5, EC-Earth3, EC-Earth3-Veg, GFDL-CM4, GFDL-ESM4, IPSL-CM6A-LR, MPI-ESM1-2-HR, NESM3.

Mouginot et al., 2014). Thus, the assumption of an ice sheet at equilibrium may be a poor assumption for the Amundsen sector. Therefore, we ran a set of synthetic experiments targeting the Amundsen region, **[described in detail in Section 2.4. [[]Using**
375 **a similar methodology as with the CMIP6-forced runs, we started with the 25-member spun-up ice sheet ensemble as the initial ice sheet states. We then ran three different forward experiments where TF anomalies are applied to just the Amundsen region (all other regions keep zero TF anomaly in the forward runs). In the Amundsen, the anomaly starts at zero and then ramps up linearly for the first 100 years to a maximum TF anomaly of 1°C, 1.5°C and 2°C. Once this maximum is reached, the anomaly is held constant for another 400 years.]**

380   We find that the differences between the 1°C and 1.5°C experiments are fairly minimal over the course of the whole experiment, with the final SLR reaching only ∼100 mm and ∼200 mm respectively (Figures 13 and A9). The 2°C experiment, however, generates over 1.2 m of SLR by the end of the simulation. This indicates almost a 12-fold increase in sea level contributions between the 1°C and 2°C experiments after about 500 years. Such a large disparity in mass loss between experiments only appears after several hundred years of run time. For example, in year 100, the difference between the SLR contributions
385 for the 1°C and 2°C experiments is only two-fold (∼15 mm and ∼30 mm respectively). From 250-350 years, the 2°C experiment shows the greatest acceleration in sea-level contributions (Figure 13). This lag between forcing and sea-level rise is expected, as it has been shown that ice shelf thinning takes place before cumulative mass loss is observed (Hoffman et al., 2019; Jenkins et al., 2018; Mouginot et al., 2014). We suspect that the rapid acceleration of mass loss after year 300 in the 2°C experiment is mostly related to MISI activation, and is exacerbated as the ice ungrounds from high topographic seafloor points
390 (Fig. 14).

     Despite stronger regional forcing than in the CMIP6 runs, the correlation between γ_0 and SLR in the synthetic Amundsen runs is not as strong as that seen in the Ross and Weddell regions in the CMIP6-forced runs. Instead, a shift in mass loss rates is observed when γ_0 and p surpass certain threshold values, similar to that in the CMIP6-forced runs **[illustrated in Figure ??]**.

[In ~~this basin~~ the Amundsen, when $p > 0.6$**,]** SLR tends to increase with higher p. **[~~, while there is no apparent dependence~~ ~~when~~ ~~$p < 0.6$.~~]** There also appears to be a threshold in γ_0 at around 5×10^6. Below this value, SLR is modest and does not change much as γ_0 varies, while above this threshold the ice sheet loses mass quickly as γ_0 increases. This is particularly evident when the TF anomalies are large enough to overcome the TF correction during the spin-up (2°C).

To get a sense of the physical behavior of the ice in the Amundsen during these experiments, we can look at the grounding line retreat over time for a low (~115 mm) and high (~1.1 m) mass loss case under 2°C TF anomaly (Figure 14). In the low mass loss case, even with a large TF anomaly, mass loss remains minimal if p and γ_0 are low. Under high p and γ_0 values, SLR contributions increase dramatically. In order to achieve a large sea level contribution, the grounding line must be pushed past some key pinning points of high local seafloor topography. Similar behavior near pinning points is noted in the CISM runs in Lipscomb et al. (2021) and in other ice sheet models such as the Ice Sheet System Model (ISSM) (Robel et al., 2019), MPAS-Albany Land Ice (MALI) model (Hoffman et al., 2019), and the adaptive-mesh BISICLES model (Waibel et al., 2018). Grounding line retreat in their Amundsen experiments (under different melt rate parameterizations) exhibits threshold behavior. In our runs, under sufficient forcing and specific parameter settings (**[~~$p > 0.6$~~ high p]** and $\gamma_0 > 5 \times 10^6$), the ice is responsive enough that the grounding line can retreat past points of high bed topography, leading to widespread ice sheet collapse that adds another ~1 meter to sea level. In our 2°C experiment, seven of the 25 **[~~p and γ_0~~ ~~combinations~~ experiments]** result in Amundsen collapse to varying extents, all contributing more than half a meter to SLR. Of these, all have **[~~$p > 0.6$~~ high values of p]** and $\gamma_0 > 4.8 \times 10^6$. **[(An additional 2°C experiment with a low p/high γ_0 combination (as in Fig. A1) did not lead to Amundsen collapse within 500 years.)]**
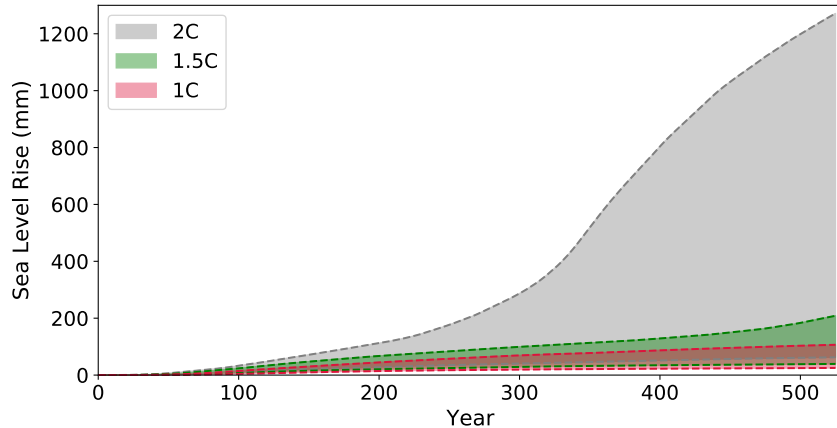
Figure 13. Range of sea level rise for all ensemble members, shading color indicates the **[synthetic]** thermal forcing experiment.

[

3.2.1 Thwaites instability and collapse on longer timescales in the 2°C synthetic framework

]
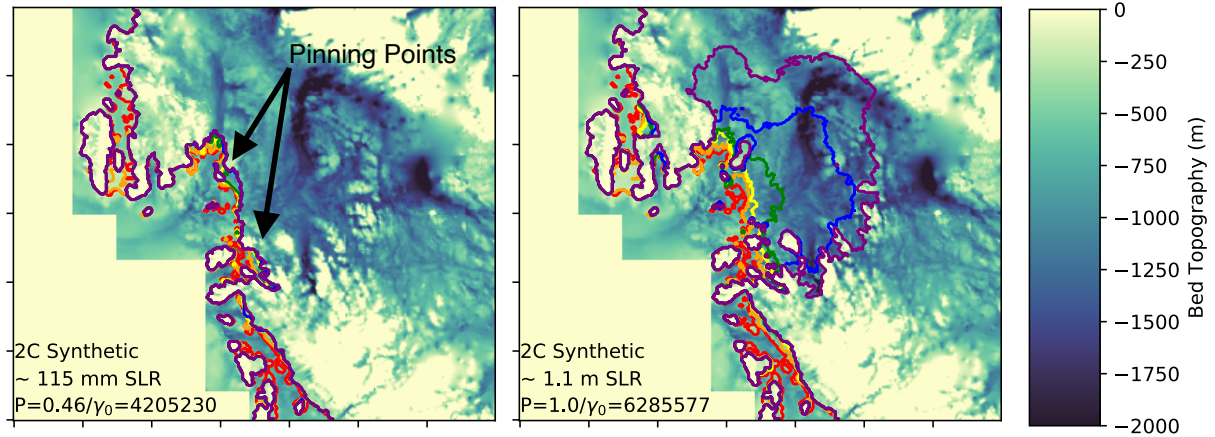
Figure 14. Grounding line location evolution over the 2°C synthetic run for (a) $p = 0.46$ / $\gamma_0 = 4205230$ and (b) $p = 1.0$ / $\gamma_0 = 6285577$. Red, orange, yellow, green, blue, purple contours indicate years 0 to 525 at roughly 100 year intervals. Shaded background shows seafloor topography (m). Negative values indicate below sea level. Note that the ice in this area is largely grounded below sea level.

[Given the large TF correction in the Amundsen region ($\delta T_{Amundsen} \sim$ **-2°C**), a 2°C warming is only enough to return conditions to present-day observed thermal forcing. Therefore, the 2°C synthetic warming experiments in the ASE can be viewed as committed-SLR experiments under current TF. As such, it is of interest to extend these simulations beyond 500 years to distinguish the stable runs from those with delayed collapse. In this way, we aim to identify the parameter space for Thwaites instability under 'current' TF conditions. To reduce computing time, we chose to extend the runs of a subset of p and γ_0 values (Table 5).]

Extended Cases							
p	0.15	0.54	0.6	0.7	0.74	0.96	0.98	1.0
γ_0 (m/s)	2954923	5175963	1560081	5321878	8654548	4849305	1710386	6285577

Table 5. [Combinations of p and γ_0 used in the subset of extended simulations.]

[Thwaites collapse begins within 1500 years in all but one ensemble member. Once the grounding line retreats past some key pinning points (shown in Fig. 14), MISI-type collapse sets in. This builds on the findings in Lipscomb et al. (2021) which, in a more limited set of p and γ_0 parameter combinations, found Thwaites collapse within 500 years only for $p = 1$. Our extended simulations show that there are, in fact, a wide range of p and γ_0 values that generate eventual Thwaites collapse. This MISI-type collapse has a characteristic timescale of about two to three centuries, but the period before collapse can be more than 500 years (Fig.15(a)). The pre-collapse period lasts until the grounding line reaches the pinning points associated with SLR of $\sim$130 mm. The case without collapse has a moderate p ($p = 0.6$) and the lowest γ_0 in our ensemble ($\gamma_0 = 1560081$). We extended this case as far as 9000 years and found that the GL stabilizes
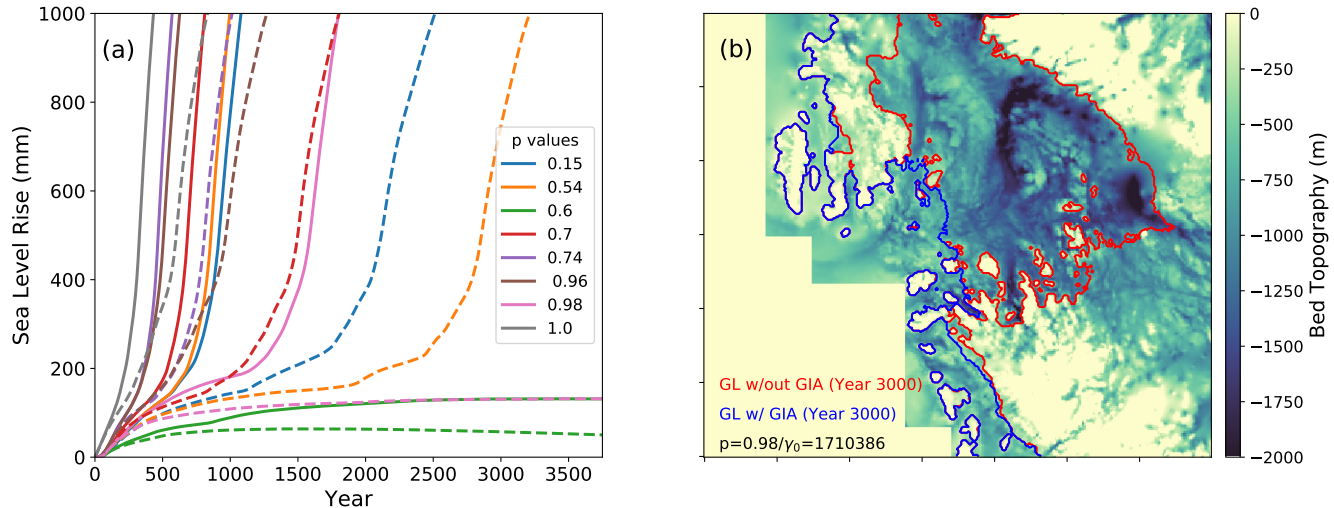
Figure 15. [(a) Sea level rise for eight extended simulations with (dashed lines) and without (solid lines) a GIA model. The y-axis is truncated at 1 m sea level rise to emphasize GIA-related delays of several centuries. (b) Amundsen region grounding line location evolution over the **2°C** synthetic run for $p = 0.98 / \gamma_0 = 1710386$ without GIA (red) and with GIA (blue) after 3000 years of simulation time. The shaded background shows seafloor topography (m) without isostatic adjustment. Negative values indicate a bed below sea level.]

on topographic pinning points about 3000 years into the simulation, and remains in this position for the rest of the
simulation.]

[We also ran extended simulations with glacial isostatic adjustment (GIA) enabled. CISM has an elastic lithosphere–relaxing asthenosphere (ELRA) model (Le Meur and Huybrechts, 1996), which represents vertical bed adjustments under a changing ice load. The runs with GIA test whether isostasy can prevent instabilities in some cases, or if it simply delays the process. With relaxation time scales (100 yr) and lithosphere rigidity (4×10^{22} N m) characteristic of WAIS (Coulon et al., 2021; Book et al., 2022), we find that GIA nearly always delays, but does not prevent, Thwaites collapse (Fig. 15(a)). The length of delay ranges from 300–800 years and depends on the p/γ_0 values and the specified SLR threshold. In only one extended scenario ($p = 0.98, \gamma_0 = 1710386$) does GIA prevent Thwaites collapse. Here again, the grounding line stabilizes on high pinning points (Fig. 15(b)), and the TF is too low to drive further grounding line retreat. This case has the second lowest γ_0 in our ensemble.]

[

3.2.2 On the coulomb basal sliding coefficient

]

[This study uses a basal sliding law that allows both power-law and Coulomb behaviors. In our spin-ups, we inverted for the power-law coefficient C_p, keeping the Coulomb parameter C_c fixed at 0.5. This value of C_c results in spun-up states that match observations well. However, C_c is not necessarily spatially uniform, and its value can influence the length of the transition zone (the zone where basal sliding transitions from power-law to Coulomb behavior). Leguy (2015) (chapter 7.1.4) showed that C_c has limited impact for small p, but influences the length of the transition zone when $p \geq 0.5$. We therefore ran additional spin-ups with low γ_0 to assess the influence of C_c on ice retreat. With $p = 0.98$ and $\gamma_0 = 1710386$, we tested $C_c = 0.25$ and $C_c = 0.1$. (With $C_c < 0.1$, there is widespread WAIS thinning inconsistent with observations.)]

[We find that lowering C_c has a limited impact in simulations with CMIP6 climate forcing (Figure A10); γ_0 remains the dominant parameter. In the 2°C synthetic experiment, however, we find that a high p/low γ_0 combination with $C_c = 0.1$ leads to a similar sea-level response compared to high p/high γ_0 and $C_c = 0.5$. Thus, lowering C_c makes the Amundsen region more prone to retreat. We recommend further study of the sensitivity to C_c in this region. We also suggest inverting for C_c, either instead of or in addition to C_p, when using Eq. 3 or similar sliding laws. To this end, work is underway to study new spin-up strategies using the sliding law proposed in Zoet and Iverson (2020), which includes a parameter analagous to C_c but not C_p.]

4 Discussion

Our primary (SSP5-8.5) CMIP6-forced CISM ensemble, consisting of 325 members (13 GCMs × 25 p and γ_0 combinations), highlights the continuing challenge to constrain uncertainties in Antarctic contributions to sea level, particularly on multi-century timescales. Depending on the magnitude of the TF anomaly and the ice sheet–ocean parameter settings, the final SLR ranges from a minimum of ~50 mm to a maximum of more than 3 m **[after 500 years]**. In all these runs, mass loss is dominated by melt from the Weddell and Ross regions. In some cases, the EAIS makes a moderate sea level contribution, while the AP contributes the least, with no more than 10 mm under any AOGCM forcing. **[~~Perhaps surprisingly, none of these simulations has significant contributions from the Amundsen, with maximum sea level contributions of ~0.5 m after 500 years.~~] [Perhaps surprisingly, most of these simulations do not have large contributions from the Amundsen region.]**

The strong dependence on γ_0 in the Ross and Weddell indicates more vulnerability to changing ocean conditions than to basal ice conditions in these regions. Mass loss is roughly proportional to the TF anomaly, although within a certain parameter space (**[~~$p < 0.6$ and~~]** $\gamma_0 < 5 \times 10^6$), mass loss remains modest. Only above **[~~these thresholds in p and γ_0~~ this threshold]** does mass loss become significant. The Ross and Filchner-Ronne (in the Weddell) are both currently cold-cavity shelves (Rignot et al., 2013; Dinniman et al., 2016), and sub-shelf melt rates are limited by weak TF at the grounding line. Once warm water enters these cavities, melt rates increase drastically. Both shelves have the potential to release vast quantities of grounded ice into the ocean. Other modeling studies have indeed illustrated the potential for the Filchner-Ronne cavity to flip between 'cold' and 'warm' states (Hazel and Stewart, 2020; Hellmer et al., 2017; Naughten et al., 2021), causing an order-of-magnitude

increase in sub-shelf melt rates and subsequent sea level contributions (Siahaan et al., 2021). We find that EAIS mass loss also correlates better with γ_0 than p, particularly when forced by warmer AOGCMs, suggesting more sensitivity to ocean warming than ice parameters. **[We note that changes in p (a model-internal parameter) are partly compensated by the subsequent calibration of the basal friction parameter, C_p. Compensation is also possible for γ_0 (a forcing-related parameter) via the δT_{sector} correction factor. However, γ_0 directly links ocean temperature changes to mass loss. It is therefore consistent that γ_0 has a more direct control on ice loss when the ocean warms.]**

By contrast, the Amundsen sector sea-level contribution is sensitive to a combination of ice sheet and ocean parameters. Under CMIP6-forced forward runs, the Amundsen response is generally modest, and grounding lines do not retreat significantly. Even under these generally weak AOGCM forcings, the Amundsen exhibits a change in mass loss rates taking it from an unresponsive to a modestly responsive region when **[$p > 0.6$ and]**$\gamma_0 > 5 \times 10^6$. When $p < 0.6$ and $\gamma_0 < 5 \times 10^6$, regional sea-level contributions barely exceed 100 mm after 500 years, even for the warmest AOGCM. In this parameter space, varying p and γ_0 has almost no effect on sea-level contributions. Only above these parameter thresholds is sea-level rise affected by increasing p or γ_0. For the coldest AOGCM, sea level decreases by the end of the simulations (i.e., there is net ice growth).

Given an individual forcing, the choice of p and γ_0 has the potential to significantly affect sea-level predictions. At most, **[for a given future forcing,]** we find a difference of **[up to about]** 0.2 m **[by the end of this after a century]**, depending on the parameters chosen at spin-up. While this mass loss is not as drastic as, say, the difference between WAIS stability and WAIS collapse, it would still pose substantial challenges for policy-making and coastal planning. The downstream effects of these parameter choices amplify on multi-century timescales. The final (500-year) SLR prediction varies by up to ~2 m depending on the spin-up parameter choices. Most of this difference arises from mass loss in the Ross and Weddell region **[(Fig A2)]**, and γ_0 is the strongest predictor of such differences on multi-century timescales. That said, the final SLR sensitivity to p and γ_0 scales similarly across all model forcings. In other words, no matter the magnitude of ocean forcing, p and γ_0 alone can generate a 2–3 fold change between the highest and lowest SLR contribution after 500 years. We reiterate that because we did not use a physically meaningful prior for our p and γ_0 ensemble, these predicted SLR ranges should not be over-interpreted.

The inversion procedure during spin-up gives large negative temperature corrections for the Amundsen sector, and therefore the sensitivity of the Amundsen sector is likely underestimated. Because the CMIP6 forcing is too weak to compensate for the large negative TF correction in the Amundsen, this forcing generates minimal mass loss compared to the Weddell and Ross. However, the 2°C synthetic simulation overcomes this TF correction, and under the same high p and γ_0 combinations found in the CMIP6-forced runs, triggers a significant Amundsen collapse **[within 500 years]**. We find that partial Thwaites collapse within 500 years (at least an additional 0.5 m of SLR) is possible only when $p > 0.6$, suggesting that partial to full water-pressure support at the grounding line promotes such a collapse. This may **[also]** be model dependent, as Hoffman et al. (2019) were able to generate Thwaites collapse with a linear basal friction law and full water-pressure support using a different ice sheet model. Furthermore, γ_0 must be greater than about 5×10^6 m/s to trigger a MISI-type instability in these simulations. Any lower γ_0 value fails to initiate collapse of any WAIS ice shelf within the modeled 500 years. The synthetic experiments in the Amundsen also illustrate a threshold of instability in the range of 1.5-2°C (with respect to the end of spin-up). This is consistent with the modeling results in Lipscomb et al. (2021) and Rosier et al. (2021), who found similar temperature

thresholds for Amundsen-region collapse. This temperature threshold is likely associated with topographic pinning points. Pinning points promote ice-sheet stability by acting as an obstacle to ice shelf flow (Still et al., 2019). Our runs show that in the Amundsen, **[high seafloor ridges slow ice retreat by allowing the ice to remain grounded for longer.]** However, under sufficient TF, the ice ungrounds, enabling unfettered retreat.

[In several extended 2°C runs, we show that the grounding line can reach critical overdeepenings if given enough time. For all p/γ_0 cases except one with very low γ_0, Thwaites collapse is initiated within 1500 years. These runs were done without isostatic feedback, whereas GIA can significantly modify sea-level projections in the Amundsen and other WAIS sectors (Kachuck et al., 2020). Larour et al. (2019) showed that with GIA included, the sea-level contribution from the Amundsen sector was reduced by 20-40% over 250 years. We therefore ran a subset of extended 2°C runs with ELRA isostasy. We found that GIA can delay Thwaites collapse by several centuries, but in most cases collapse remains inevitable. More sophisticated isostasy models would be needed to fully probe GIA impacts on grounding-line stabilization. These extended experiments do not alter the conclusions of the main ensemble of shorter experiments; γ_0 is more important than p for committed SLR.]

We note a number of caveats and assumptions. First, the AOGCM ocean models used to generate our TF generally have low resolution and do not include ice shelf cavities. By assuming that the far-field temperatures can be extrapolated under the shelves, we are missing complex processes and potential feedbacks that shape the sub-shelf cavity circulation and affect melt rates (e.g., time scales of cavity circulation (Snow et al., 2017; Naughten et al., 2019)). For example, once warm water flushes the ice shelf cavities, a positive meltwater feedback can enhance the shelf circulation and the onshore transport of open ocean heat (Hellmer et al., 2017). This would limit our ability to identify such a tipping point without resolving the sub-shelf circulation. Furthermore, the extrapolation of far-field thermal properties into current cold shelf cavities like the Filchner-Ronne and Ross regions may bring an unrealistic amount of heat to grounding lines, overestimating mass loss in these regions (Daae et al., 2020; Naughten et al., 2021).

Without explicitly representing sub-shelf circulation, we have assumed a simple quadratic relationship between TF and melt rates. This melt rate parameterization cannot capture critical processes that transport warm water to grounding lines, such as topographic steering along bed troughs (Nakayama et al., 2018). Due to limited computing resources, we have explored only one such form (non-local slope), and we only consider the SSP5-8.5 forcing scenario (Meinshausen et al., 2020). **[We neglect other physical processes, such as MICI and atmospheric changes, and our resolution of 4 km is too coarse to capture all grounding-line processes. Also, the simple no-advance calving criterion may underestimate the effects of basal melting on calving-front retreat and buttressing of grounded ice.]**

Another consideration is the AOGCMs themselves, and the limitations in their representation of high-latitude ocean dynamics. All CMIP6 models used to force these simulations have temperature and salinity biases, particularly in the Southern Ocean (Beadling et al., 2020). The ocean resolution is typically too low to resolve major features such as the Antarctic Slope Current, eddies and tides, ice shelves, and polynyas (Purich and England, 2021; Mack et al., 2019). All these features have the potential to affect sub-shelf melt rates. For example, Naughten et al. (2018) found that Weddell polynyas have an effect on the Filchner-Ronne cavity temperatures and melt rates since they determine the salinity and density of the cavity source waters. As

a result, polynya formation, not resolvable in CMIP6 models, impacts the circulation strength and the melt rates. Finally, since these models are not coupled to the ice sheet, we do not account for meltwater feedbacks.

To overcome many of these issues, it is necessary to better represent sub-shelf circulation and to couple the ocean and ice sheet. While some modeling centers have coupled an interactive Greenland Ice Sheet with an AOGCM, only a few have included ice shelf cavities around Antarctica (e.g., UKESM (Siahaan et al., 2021) and E3SM (Comeau et al., 2022)). CESM developmental code supports a coupled Antarctic ice sheet, but has yet to be validated as of this writing. CESM is also switching to the MOM6 ocean model (Adcroft et al., 2019), which can resolve sub-shelf circulation. It is likely that the ice sheet modeling community will eventually shift away from the constraints of these sub-shelf melt parameterizations.

5 Conclusions

In this study, we expand the scope of previous ISMIP6-style simulations by probing in greater detail the dependence of future Antarctic mass loss on two important parameters: p (which affects basal friction near the grounding line) and γ_0 (which **[controls]** the sub-shelf melt rate). By virtue of the spin-up methodology, these parameter settings can condition the ice sheet to be more or less susceptible to ocean thermal forcing, which has significant implications for sea-level projections. We run a 325-member CISM ensemble, where 25 unique combinations of p and γ_0 are used to generate new spin-ups, each achieving similar spun-up states that are in steady state and whose ice sheet configuration (e.g., ice thickness and velocities) resembles today's ice sheet. **[These spin-ups do not, however, represent the transient state of the AIS, since the current ice sheet is not in equilibrium (particularly in the Amundsen region). Rather, the ice sheet is spun up to a modern configuration, and these simulations are designed to probe the sensitivity of the AIS around this reference state.]**

Each spun-up state is run forward, forced with regionally-averaged ocean TF anomalies derived from 13 different CMIP6 models. The thermal anomalies are ramped up linearly for 100 years from the 1995-2005 mean to the 2090-2100 mean, after which they are held constant for 400 years. Our study is novel in that we have identified the parametric **[(p and γ_0)]** thresholds necessary for triggering widespread mass loss **[within 500 years]**. We find that with the combination of low basal friction near the grounding line (**[$p > 0.6$ moderate to high p]**), high sensitivity of melt rates to TF ($\gamma_0 > 5 \times 10^5$), and sufficient TF anomalies, mass loss becomes significant in multiple basins. **[~~These thresholds~~ This threshold in p ~~and γ_0~~ ~~tend~~ tends]** to hold for all major WAIS basins (Amundsen, Ross and Weddell). The choice of p and γ_0 alone can impact final (500-year) sea level estimates by up to 2 m. The differences are less extreme after 100 years, but still significant, with parameter settings impacting SLR estimates by up to 0.2 m. The Ross and Weddell regions dominate the sea-level contributions in CMIP6-forced forward simulations. Mass loss in these areas is largely controlled by γ_0 rather than p, implying dominance of ocean forcing parameters over ice-sheet parameters. The Amundsen region exhibits a mix of ocean, ice, and temperature thresholds that together determine the sensitivity.

The CMIP6-forced runs fail to produce widespread WAIS collapse after 500 years by virtue of relatively weak forcing in the Amundsen. However, with additional synthetic forcing, we find that large Amundsen mass loss can be triggered with TF anomalies between 1.5 and 2°C. In these cases, the grounding line retreats from topographic pinning points. Without these

stabilizing points, the grounded ice in the basin collapses. **[Collapse sometimes begins well after year 500, but proceeds quickly once under way, with a characteristic time scale of two or three centuries. Adding GIA feedbacks in extended simulations can delay Amundsen collapse by several centuries, but in most cases does not prevent eventual collapse.]**

Our study highlights the potential downstream effects of ice conditioning during model spin-up. Since it is possible to achieve a similar spun-up state with different sensitivities to ocean warming, it is imperative to understand the effects of the most influential ice and ocean parameters. Current ice sheet models have difficulty making predictions about Antarctic mass loss, especially on multi-century timescales. More work is necessary to make realistic projections. The sensitivity to model parameters demonstrated in our experiments emphasizes the need to impose better constraints on model initial conditions by using observational constraints for ice sheet transient behavior.

Code and data availability. Code and Data are available at: https://github.com/mberdahl-uw/SpinUp_Paper.git

Appendix A

 A1
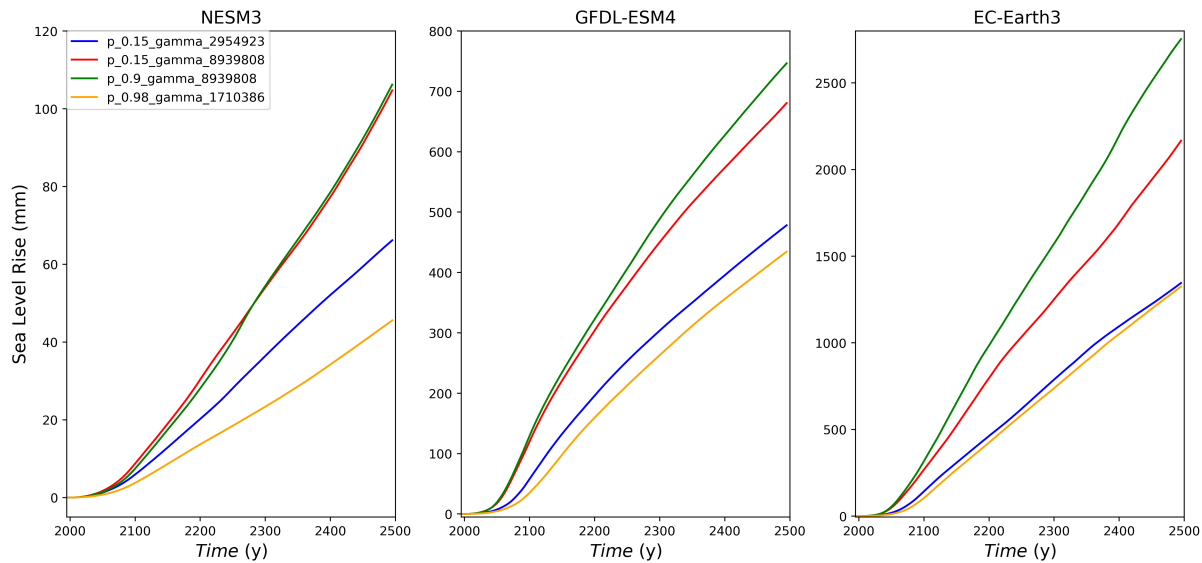
Figure A1. [Sea level rise experiment using low (NESM3, left panel), moderate (GFDL-ESM4, center panel), and high (EC-Earth3, right panel) CMIP6 climate scenarios, showing results using p/γ_0 values that are low/low (blue), low/high (red), high/high (green), and high/low (orange). The results show: (1) with low p and high gamma the sea-level response is similar compared to the high p and high γ_0 combination for low and moderate forcing; (2) p does influence the results under high forcing scenarios; (3) the sea-level response with low p and high γ_0 is always larger compared to the response with high p and low γ_0 highlighting the strong influence of γ_0.]
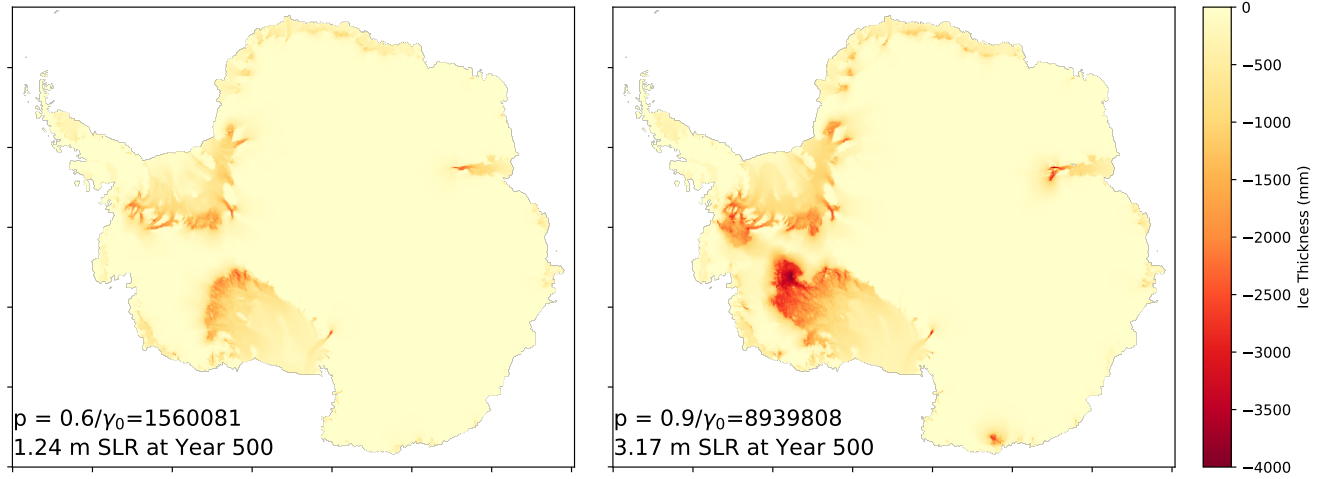
Figure A2. Thickness change between beginning and end of simulation for two simulations run with EC-Earth3-Veg. The only difference between these simulations is the p and γ_0 settings during spin-up. Resulting sea level contributions at year 500 differ by over 2 m. The majority of mass loss occurs in the Weddell and Ross regions.
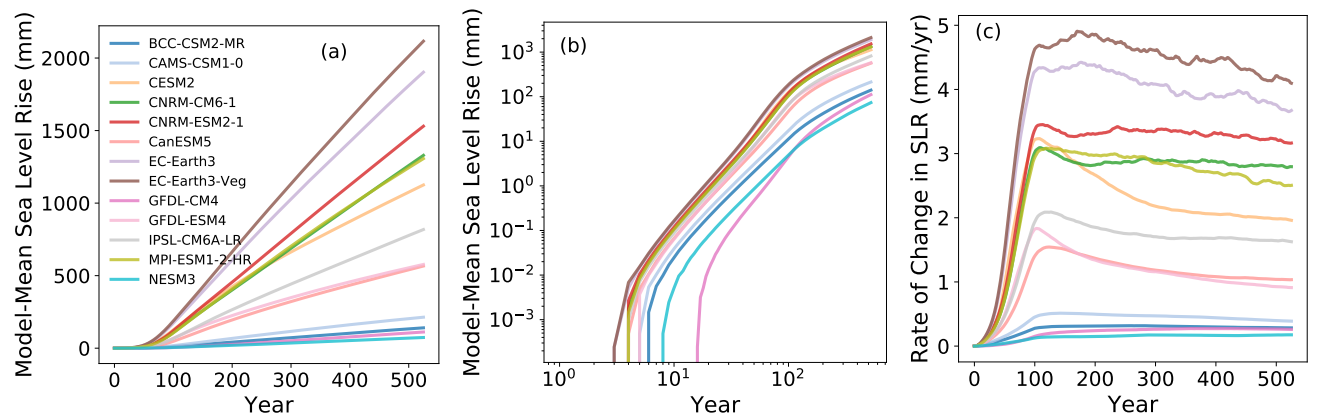
Figure A3. (a) Model-mean sea level rise, (b) Model-mean sea level rise on log-log scale and (c) Model-mean SLR rate of change (mm/yr).
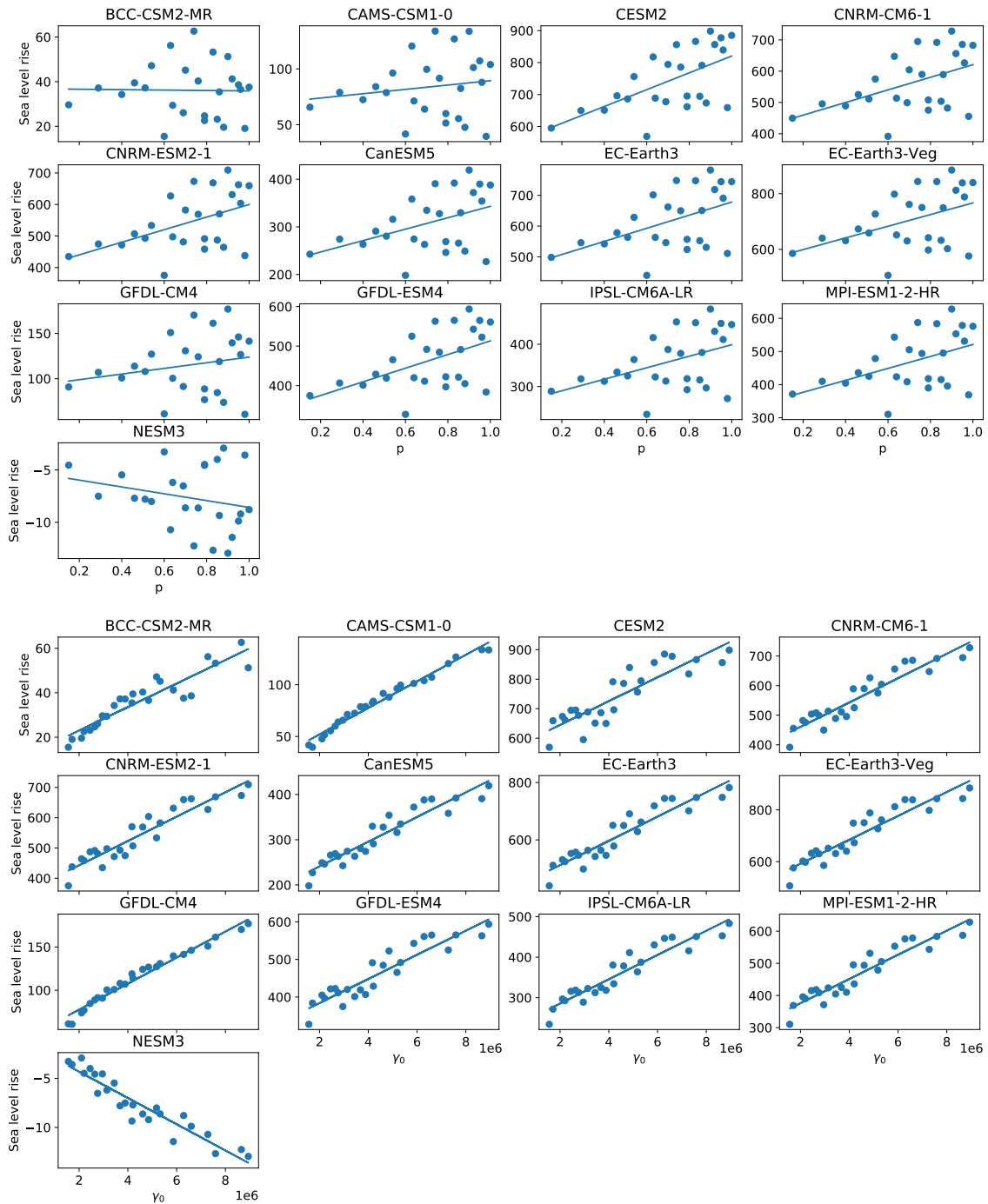
Figure A4. SLR as a function of p and γ_0 in the Weddell region.
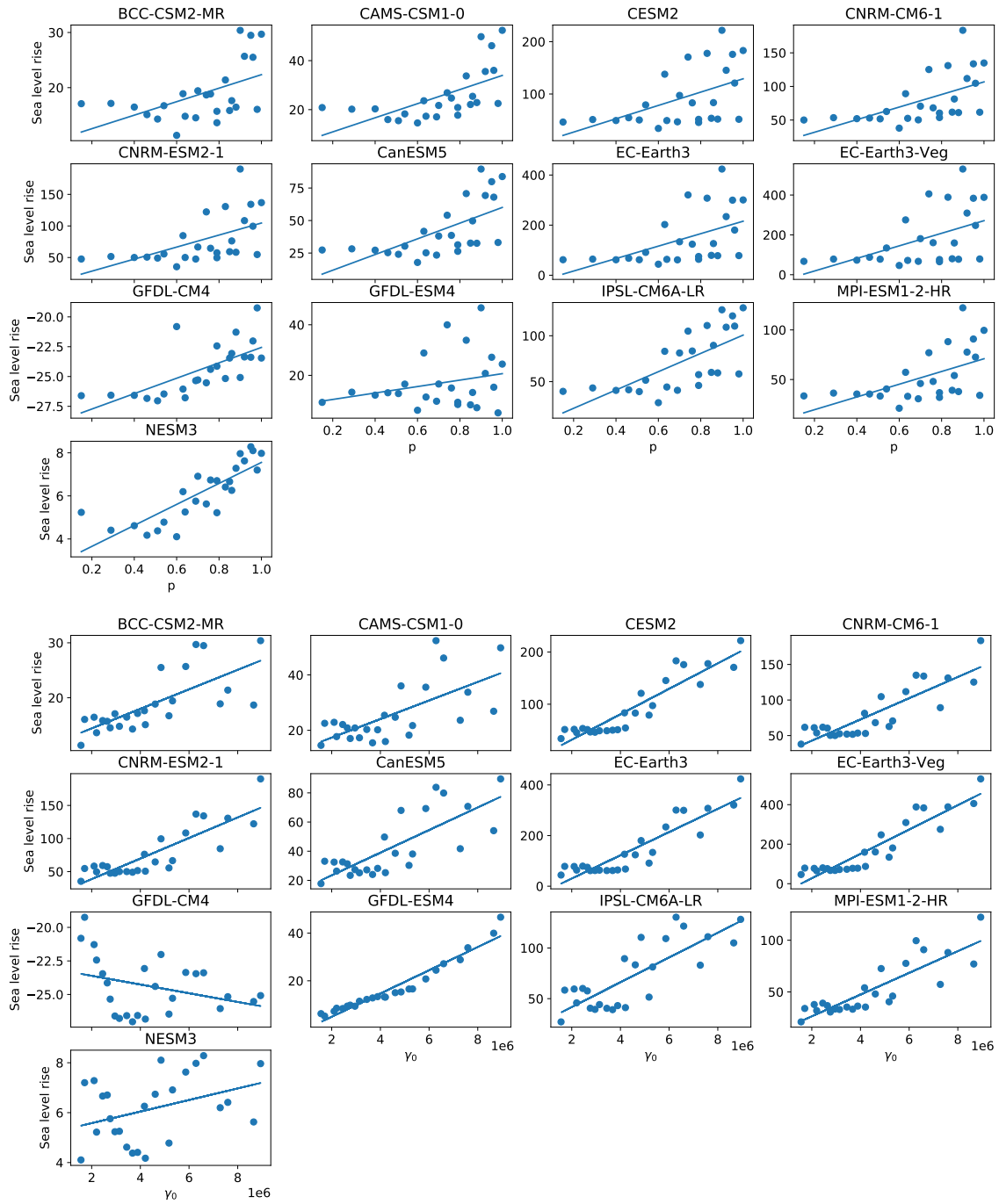
Figure A5. SLR as a function of p and γ_0 in the Amundsen region.
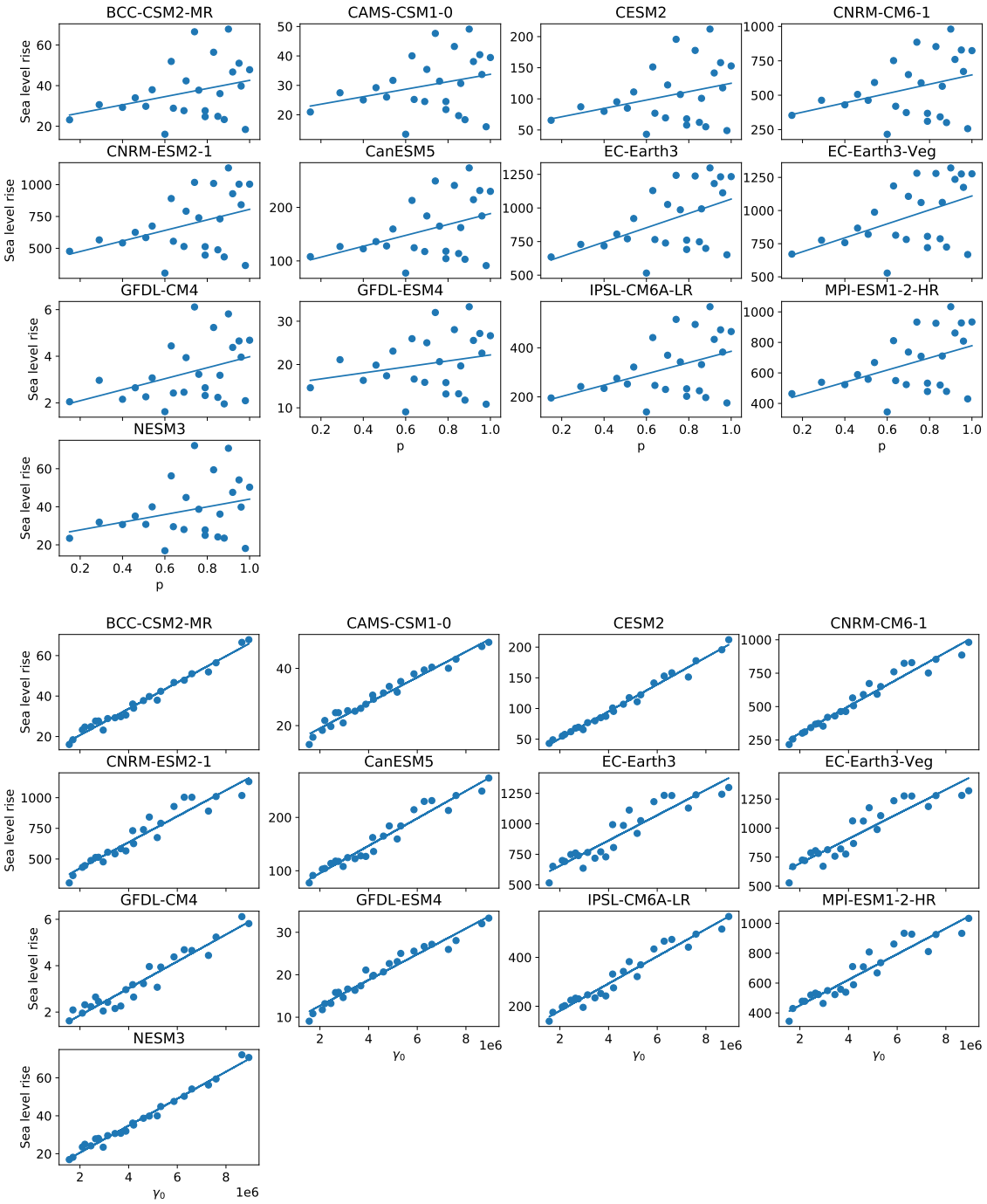
Figure A6. SLR as a function of p and γ_0 in the Ross region.
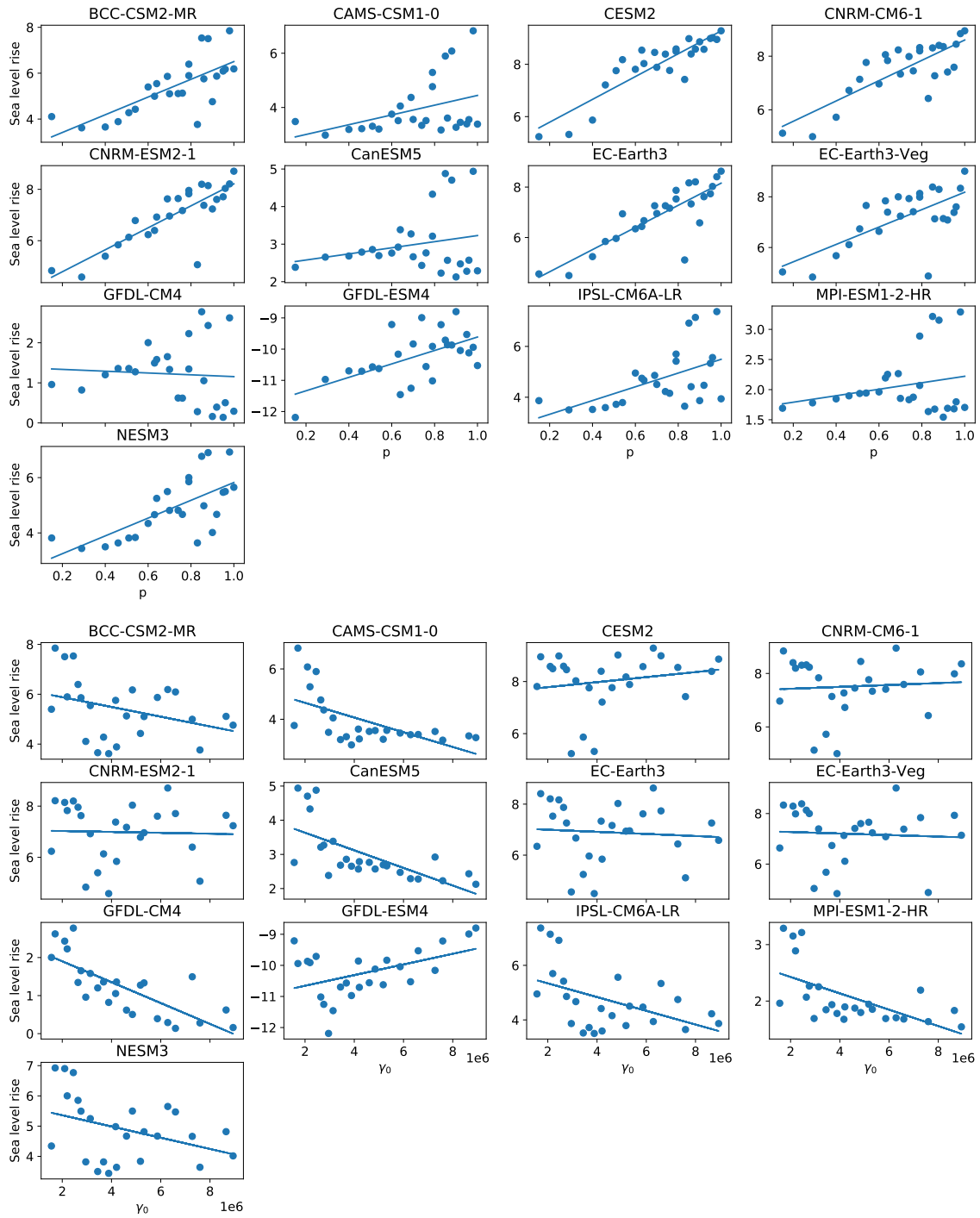
Figure A7. SLR as a function o p and γ_0 in the Peninsula (AP) region.
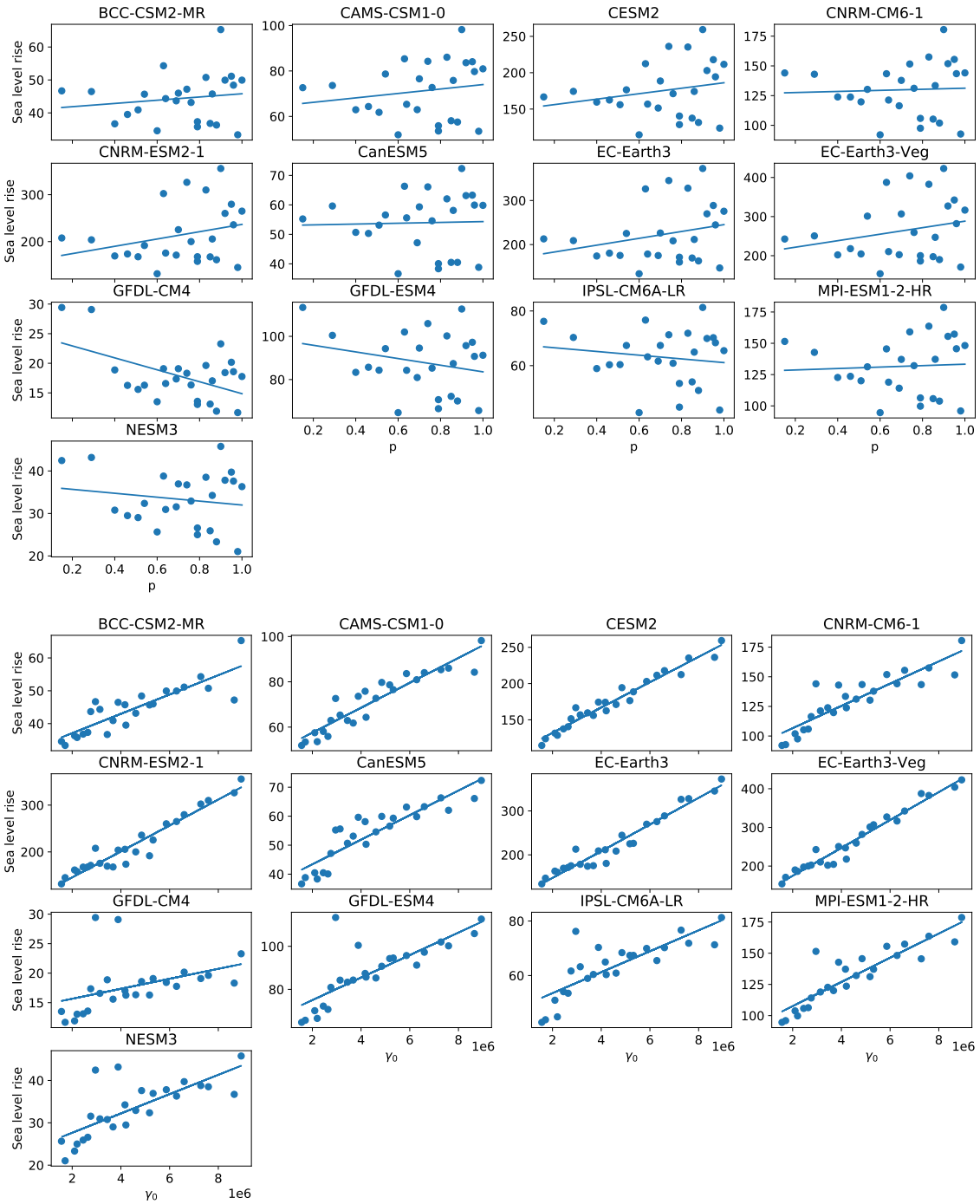
Figure A8. SLR as a function of p and γ_0 in the East Antarctic (EAIS) region.
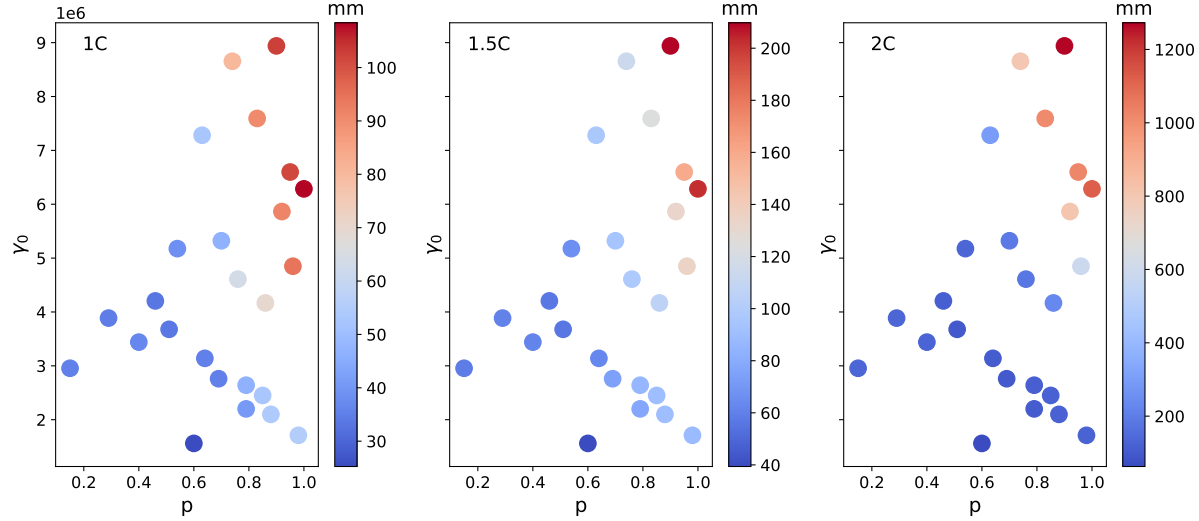
Figure A9. Final (500 year) sea level contribution from the Amundsen under three different synthetic forcing scenarios as a function of γ_0 vs p. The panels correspond to the three experiments: 1°C (left), 1.5°C (middle) and 2°C (right). Note the different colorbar scales.

[~~Final Minimum and Maximum~~ SLR values after 500 (100) years of simulation]				
CMIP6 Model Name	Min Final SLR (mm)	Max Final SLR (mm)	Diff Final SLR (mm)	Ratio (Max:Min) Final SLR
BCC-CSM2-MR	82.72 [(6.99)]	218.24 [(15.94)]	135.52 [(8.95)]	2.6 [(2.28)]
CAMS-CSM1-0	125.12 [(9.91)]	332.82 [(25.86)]	207.7 [(15.95)]	2.6 [(2.6)]
CESM2	768.69 [(55.98)]	1599.16 [(202.19)]	830.471 [(146.21)]	2.08 [(3.61)]
CNRM-CM6-1	744.51 [(44.33)]	2080.16 [(184.63)]	1335.65 [(140.3)]	2.79 [(4.16)]
CNRM-ESM2-1	853.84 [(50.95)]	2392.35 [(205.54)]	1538.51 [(154.59)]	2.8 [(4.03)]
CanESM5	332.52 [(19.83)]	855.8 [(84.84)]	523.28[(65.01)]	2.57 [(4.28)]
EC-Earth3	1139.45 [(77.85)]	2881.83 [(279.37)]	1742.38 [(201.52)]	2.53 [(3.59)]
EC-Earth3-Veg	1241.82 [(85.10)]	3165.48 [(300.54)]	1923.66 [(215.44)]	2.55 [(3.53)]
GFDL-CM4	56.75 [(2.27)]	179.89 [(7.65)]	123.14 [(5.38)]	3.16 [(3.37)]
GFDL-ESM4	398.05 [(28.90)]	776.32 [(113.7)]	378.27 [(84.8)]	1.95 [(3.93)]
IPSL-CM6A-LR	447.69 [(27.59)]	1262.62 [(118.49)]	814.93 [(90.9)]	2.82 [(4.29)]
MPI-ESM1-2-HR	772.16 [(42.85)]	1962.88 [(182.37)]	1190.72 [(139.52)]	2.54 [(4.26)]
NESM3	47.58 [(3.26)]	114.27 [(6.36)]	66.69 [(3.1)]	2.4 [(1.95)]

Table A1. [~~Final~~]SLR values [~~(end of 500 years of simulation)~~ after 500 (100) years of simulation] for each climate model ensemble showing the minimum, the maximum, the difference, and the ratio between the maximum and minimum. Brackets show values for year 100 years after simulation starts.]
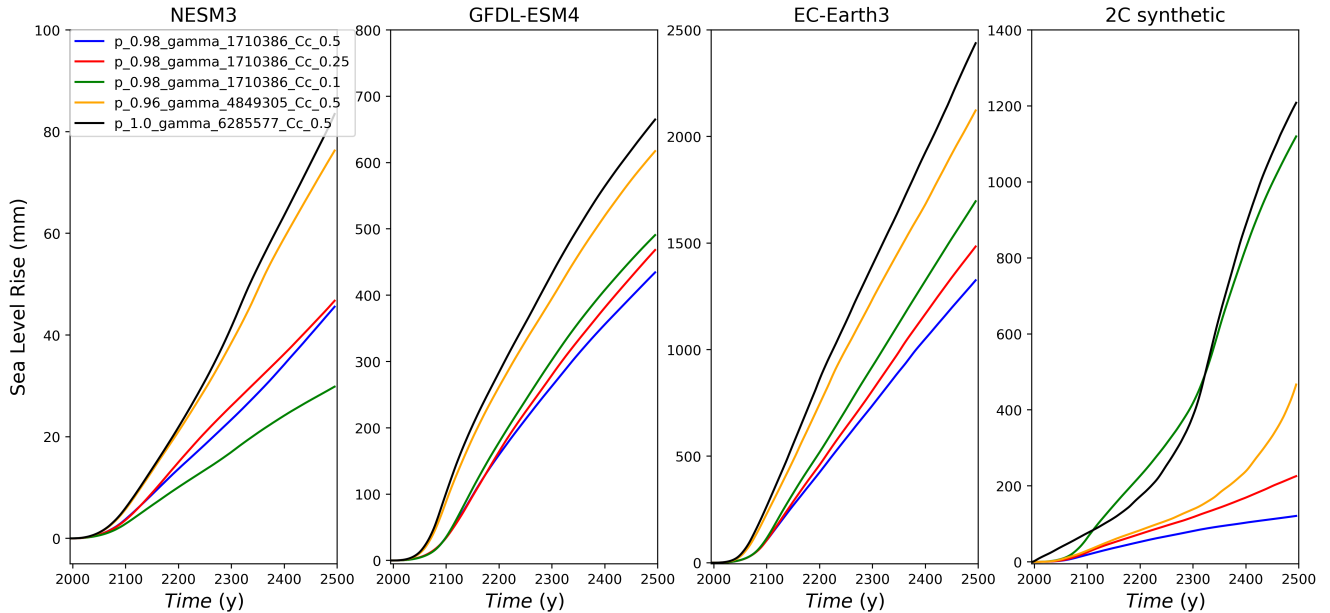
Figure A10. [**Sea level rise experiment using low (NESM3), moderate (GFDL-ESM4), and high (EC-Earth3) CMIP6 climate scenarios and 2°C synthetic experiment, showing results using high p and low γ_0 values with $C_c = 0.5, 0.25, 0.1$ (blue,red,green respectively) and high p, $C_c = 0.5$, and mid/high γ_0 values (orange and black respectively). The results show: (1) for fixed p and γ_0, lower C_c values lead to a stronger sea-level response (the exceptional behavior seen with NESM3 might be due to the low and negative TF forcing in the Amundsen region); (2) For the 3 CMIP6 forced experiments, lowering C_c by a factor of 5 is not enough to match sea level contribution produced by the set ups using higher γ_0 values; (3) in the 2°C synthetic experiment, the results with $C_c = 0.1$ leads to similar sea-level response compared with the experiment with high γ_0.**]

Author contributions. MB, GL, and WHL designed the experiments, with input and advice from NU. GL and MB staged and ran the experiments. WHL developed and provided an ice sheet spin-up. MB and GL prepared the manuscript with contributions from all co-authors.

Competing interests. The authors declare that they have no conflict of interest.

Acknowledgements. We thank Qiang Sun for providing the CMIP6 ocean model output. This work was supported by the U.S. Department

595   of Energy (DOE) Office of Science (Biological and Environmental Research), Early Career Research program, as well as National Science Foundation (NSF) Grant No. 2045075. This material is based upon work supported by the National Center for Atmospheric Research, which is a major facility sponsored by the National Science Foundation under Cooperative Agreement No. 1852977. This research used resources provided by the Los Alamos National Laboratory Institutional Computing Program, which is supported by the U.S. Department of Energy National Nuclear Security Administration under Contract No. 89233218CNA000001. Further computing and data storage resources, in-

600   cluding the Cheyenne supercomputer (doi:10.5065/D6RX99HX), were provided by the Computational and Information Systems Laboratory (CISL) at NCAR.

References

Adcroft, A., Anderson, W., Balaji, V., Blanton, C., Bushuk, M., Dufour, C. O., Dunne, J. P., Griffies, S. M., Hallberg, R., Harrison, M. J., et al.: The GFDL global ocean and sea ice model OM4. 0: Model description and simulation features, Journal of Advances in Modeling Earth Systems, 11, 3167–3211, 2019.

Asay-Davis, X. S., Cornford, S. L., Durand, G., Galton-Fenzi, B. K., Gladstone, R. M., Gudmundsson, G. H., Hattermann, T., Holland, D. M., Holland, D., Holland, P. R., et al.: Experimental design for three interrelated marine ice sheet and ocean model intercomparison projects: MISMIP v. 3 (MISMIP+), ISOMIP v. 2 (ISOMIP+) and MISOMIP v. 1 (MISOMIP1), Geoscientific Model Development, 9, 2471–2497, 2016.

Bakker, A. M., Louchard, D., and Keller, K.: Sources and implications of deep uncertainties surrounding sea-level projections, Climatic change, 140, 339–347, 2017.

Beadling, R., Russell, J., Stouffer, R., Mazloff, M., Talley, L., Goodman, P., Sallée, J.-B., Hewitt, H., Hyder, P., and Pandde, A.: Representation of Southern Ocean properties across coupled model intercomparison project generations: CMIP3 to CMIP6, Journal of Climate, 33, 6555–6581, 2020.

Berdahl, M., Leguy, G., Lipscomb, W. H., and Urban, N. M.: Statistical emulation of a perturbed basal melt ensemble of an ice sheet model to better quantify Antarctic sea level rise uncertainties, The Cryosphere, 15, 2683–2699, 2021.

Book, C., Hoffman, M. J., Kachuck, S. B., Hillebrand, T. R., Price, S. F., Perego, M., and Bassis, J. N.: Stabilizing effect of bedrock uplift on retreat of Thwaites Glacier, Antarctica, at centennial timescales, Earth and Planetary Science Letters, 597, 117 798, 2022.

Cao, J., Wang, B., Yang, Y.-M., Ma, L., Li, J., Sun, B., Bao, Y., He, J., Zhou, X., and Wu, L.: The NUIST Earth System Model (NESM) version 3: description and preliminary evaluation, Geoscientific Model Development, 11, 2975–2993, 2018.

Comeau, D., Asay-Davis, X. S., Begeman, C. B., Hoffman, M. J., Lin, W., Petersen, M. R., Price, S. F., Roberts, A. F., Van Roekel, L. P., Veneziani, M., et al.: The DOE E3SM v1. 2 Cryosphere Configuration: Description and Simulated Antarctic Ice-Shelf Basal Melting, Journal of Advances in Modeling Earth Systems, 14, e2021MS002 468, 2022.

Cornford, S. L., Seroussi, H., Asay-Davis, X. S., Gudmundsson, G. H., Arthern, R., Borstad, C., Christmann, J., Dias dos Santos, T., Feldmann, J., Goldberg, D., et al.: Results of the third Marine Ice Sheet Model Intercomparison Project (MISMIP+), The Cryosphere Discussions, 2020.

Coulon, V., Bulthuis, K., Whitehouse, P. L., Sun, S., Haubner, K., Zipf, L., and Pattyn, F.: Contrasting response of West and East Antarctic ice sheets to glacial isostatic adjustment, Journal of Geophysical Research: Earth Surface, 126, e2020JF006 003, 2021.

Daae, K., Hattermann, T., Darelius, E., Mueller, R. D., Naughten, K. A., Timmermann, R., and Hellmer, H. H.: Necessary conditions for warm inflow toward the Filchner Ice Shelf, Weddell Sea, Geophysical Research Letters, 47, e2020GL089 237, 2020.

Danabasoglu, G., Lamarque, J.-F., Bacmeister, J., Bailey, D., DuVivier, A., Edwards, J., Emmons, L., Fasullo, J., Garcia, R., Gettelman, A., et al.: The community earth system model version 2 (CESM2), Journal of Advances in Modeling Earth Systems, 12, e2019MS001 916, 2020.

DeConto, R. M. and Pollard, D.: Contribution of Antarctica to past and future sea-level rise, Nature, 531, 591, 2016.

DeConto, R. M., Pollard, D., Alley, R. B., Velicogna, I., Gasson, E., Gomez, N., Sadai, S., Condron, A., Gilford, D. M., Ashe, E. L., et al.: The Paris Climate Agreement and future sea-level rise from Antarctica, Nature, 593, 83–89, 2021.

Depoorter, M. A., Bamber, J., Griggs, J., Lenaerts, J., Ligtenberg, S. R., Van den Broeke, M., and Moholdt, G.: Calving fluxes and basal melt rates of Antarctic ice shelves, Nature, 502, 89, 2013.

Dinniman, M. S., Asay-Davis, X. S., Galton-Fenzi, B. K., Holland, P. R., Jenkins, A., and Timmermann, R.: Modeling ice shelf/ocean interaction in Antarctica: A review, Oceanography, 29, 144–153, 2016.

Döscher, R., Acosta, M., Alessandri, A., Anthoni, P., Arneth, A., Arsouze, T., Bergmann, T., Bernadello, R., Bousetta, S., Caron, L.-P., et al.: The EC-earth3 Earth system model for the climate model intercomparison project 6, Geoscientific Model Development Discussions, pp. 1–90, 2021.

Dunne, J., Horowitz, L., Adcroft, A., Ginoux, P., Held, I., John, J., Krasting, J., Malyshev, S., Naik, V., Paulot, F., et al.: The GFDL Earth System Model version 4.1 (GFDL-ESM 4.1): Overall coupled model description and simulation characteristics, Journal of Advances in Modeling Earth Systems, 12, e2019MS002 015, 2020.

Edwards, T. L., Nowicki, S., Marzeion, B., Hock, R., Goelzer, H., Seroussi, H., Jourdain, N. C., Slater, D. A., Turner, F. E., Smith, C. J., et al.: Projected land ice contributions to twenty-first-century sea level rise, Nature, 593, 74–82, 2021.

Favier, L., Durand, G., Cornford, S. L., Gudmundsson, G. H., Gagliardini, O., Gillet-Chaulet, F., Zwinger, T., Payne, A., and Le Brocq, A. M.: Retreat of Pine Island Glacier controlled by marine ice-sheet instability, Nature Climate Change, 4, 117–121, 2014.

Fox-Kemper, B., Hewitt, H., Xiao, C., Aðalgeirsdóttir, G., Drijfhout, S., Edwards, T., Golledge, N., Hemer, M., Kopp, R., Krinner, G., Mix, A., Notz, D., Nowicki, S., Nurhati, I., Ruiz, L., Sallée, J.-B., Slangen, A., and Yu, Y.: Ocean, Cryosphere and Sea Level Change, p. 1211–1362, Cambridge University Press, Cambridge, United Kingdom and New York, NY, USA, https://doi.org/10.1017/9781009157896.011, 2021.

Fürst, J. J., Durand, G., Gillet-Chaulet, F., Tavard, L., Rankl, M., Braun, M., and Gagliardini, O.: The safety band of Antarctic ice shelves, Nature Climate Change, 6, 479–482, 2016.

Goldberg, D. N.: A variationally derived, depth-integrated approximation to a higher-order glaciological flow model, Journal of Glaciology, 57, 157–170, 2011.

Gudmundsson, G. H., Paolo, F. S., Adusumilli, S., and Fricker, H. A.: Instantaneous Antarctic ice sheet mass loss driven by thinning ice shelves, Geophysical Research Letters, 46, 13 903–13 909, 2019.

Hazel, J. E. and Stewart, A. L.: Bistability of the Filchner-Ronne Ice Shelf Cavity Circulation and Basal Melt, Journal of Geophysical Research: Oceans, 125, e2019JC015 848, 2020.

Held, I., Guo, H., Adcroft, A., Dunne, J., Horowitz, L., Krasting, J., Shevliakova, E., Winton, M., Zhao, M., Bushuk, M., et al.: Structure and performance of GFDL's CM4. 0 climate model, Journal of Advances in Modeling Earth Systems, 11, 3691–3727, 2019.

Hellmer, H. H., Kauker, F., Timmermann, R., and Hattermann, T.: The fate of the southern Weddell Sea continental shelf in a warming climate, Journal of Climate, 30, 4337–4350, 2017.

Hoffman, M. J., Asay-Davis, X., Price, S. F., Fyke, J., and Perego, M.: Effect of subshelf melt variability on sea level rise contribution from Thwaites Glacier, Antarctica, Journal of Geophysical Research: Earth Surface, 124, 2798–2822, 2019.

Holland, P. R., Jenkins, A., and Holland, D. M.: The response of ice shelf basal melting to variations in ocean temperature, Journal of Climate, 21, 2558–2572, 2008.

Holland, P. R., Bracegirdle, T. J., Dutrieux, P., Jenkins, A., and Steig, E. J.: West Antarctic ice loss influenced by internal climate variability and anthropogenic forcing, Nature Geoscience, 12, 718–724, 2019.

Jenkins, A.: A simple model of the ice shelf–ocean boundary layer and current, Journal of Physical Oceanography, 46, 1785–1803, 2016.

Jenkins, A., Shoosmith, D., Dutrieux, P., Jacobs, S., Kim, T. W., Lee, S. H., Ha, H. K., and Stammerjohn, S.: West Antarctic Ice Sheet retreat in the Amundsen Sea driven by decadal oceanic variability, Nature Geoscience, 11, 733–738, 2018.

Joughin, I., Smith, B. E., and Medley, B.: Marine ice sheet collapse potentially under way for the Thwaites Glacier Basin, West Antarctica, Science, 344, 735–738, 2014.

Joughin, I., Smith, B. E., and Schoof, C. G.: Regularized Coulomb friction laws for ice sheet sliding: Application to Pine Island Glacier, Antarctica, Geophysical research letters, 46, 4764–4771, 2019.

680 Jourdain, N. C., Asay-Davis, X., Hattermann, T., Straneo, F., Seroussi, H., Little, C. M., and Nowicki, S.: A protocol for calculating basal melt rates in the ISMIP6 Antarctic ice sheet projections, The Cryosphere, 14, 3111–3134, 2020.

Kachuck, S. B., Martin, D. F., Bassis, J. N., and Price, S. F.: Rapid viscoelastic deformation slows marine ice sheet instability at Pine Island Glacier, Geophysical Research Letters, 47, e2019GL086 446, 2020.

Kopp, R. E., DeConto, R. M., Bader, D. A., Hay, C. C., Horton, R. M., Kulp, S., Oppenheimer, M., Pollard, D., and Strauss, B. H.: Evolving
685 understanding of Antarctic ice-sheet physics and ambiguity in probabilistic sea-level projections, Earth's Future, 5, 1217–1233, 2017.

Larour, E., Seroussi, H., Adhikari, S., Ivins, E., Caron, L., Morlighem, M., and Schlegel, N.: Slowdown in Antarctic mass loss from solid Earth and sea-level feedbacks, Science, 364, eaav7908, 2019.

Le Meur, E. and Huybrechts, P.: A comparison of different ways of dealing with isostasy: examples from modelling the Antarctic ice sheet during the last glacial cycle, Annals of Glaciology, 23, 309–317, 1996.

690 Leguy, G.: The effect of a basal-friction parameterization on grounding-line dynamics in ice-sheet models, New Mexico Institute of Mining and Technology, 2015.

Leguy, G. R., Asay-Davis, X. S., and Lipscomb, W. H.: Parameterization of basal friction near grounding lines in a one-dimensional ice sheet model, The Cryosphere, 8, 1239–1259, https://doi.org/10.5194/tc-8-1239-2014, 2014.

Leguy, G. R., Lipscomb, W. H., and Asay-Davis, X. S.: Marine ice sheet experiments with the Community Ice Sheet Model, The Cryosphere,
695 15, 3229–3253, 2021.

Levermann, A., Winkelmann, R., Albrecht, T., Goelzer, H., Golledge, N. R., Greve, R., Huybrechts, P., Jordan, J., Leguy, G., Martin, D., et al.: Projecting Antarctica's contribution to future sea level rise from basal ice shelf melt using linear response functions of 16 ice sheet models (LARMIP-2), Earth System Dynamics, 11, 35–76, 2020.

Lipscomb, W. H., Price, S. F., Hoffman, M. J., Leguy, G. R., Bennett, A. R., Bradley, S. L., Evans, K. J., Fyke, J. G., Kennedy, J. H., Perego,
700 M., et al.: Description and evaluation of the Community Ice Sheet Model (CISM) v2. 1, Geoscientific Model Development, 12, 387–424, 2019.

Lipscomb, W. H., Leguy, G. R., Jourdain, N. C., Asay-Davis, X., Seroussi, H., and Nowicki, S.: ISMIP6-based projections of ocean-forced Antarctic Ice Sheet evolution using the Community Ice Sheet Model, The Cryosphere, 15, 633–661, 2021.

Little, C. M., Gnanadesikan, A., and Oppenheimer, M.: How ice shelf morphology controls basal melting, Journal of Geophysical Research:
705 Oceans, 114, 2009.

Lurton, T., Balkanski, Y., Bastrikov, V., Bekki, S., Bopp, L., Braconnot, P., Brockmann, P., Cadule, P., Contoux, C., Cozic, A., et al.: Implementation of the CMIP6 Forcing Data in the IPSL-CM6A-LR Model, Journal of Advances in Modeling Earth Systems, 12, e2019MS001 940, 2020.

Mack, S. L., Dinniman, M. S., Klinck, J. M., McGillicuddy Jr, D. J., and Padman, L.: Modeling ocean eddies on Antarctica's cold water
710 continental shelves and their effects on ice shelf basal melting, Journal of Geophysical Research: Oceans, 124, 5067–5084, 2019.

McKay, M. D., Beckman, R. J., and Conover, W. J.: Comparison of three methods for selecting values of input variables in the analysis of output from a computer code, Technometrics, 21, 239–245, 1979.

Meinshausen, M., Nicholls, Z. R., Lewis, J., Gidden, M. J., Vogel, E., Freund, M., Beyerle, U., Gessner, C., Nauels, A., Bauer, N., et al.: The shared socio-economic pathway (SSP) greenhouse gas concentrations and their extensions to 2500, Geoscientific Model Development, 13, 3571–3605, 2020.

Morlighem, M., Rignot, E., Binder, T., Blankenship, D., Drews, R., Eagles, G., Eisen, O., Ferraccioli, F., Forsberg, R., Fretwell, P., et al.: Deep glacial troughs and stabilizing ridges unveiled beneath the margins of the Antarctic ice sheet, Nature Geoscience, 13, 132–137, 2020.

Mottram, R., Hansen, N., Kittel, C., van Wessem, J. M., Agosta, C., Amory, C., Boberg, F., van de Berg, W. J., Fettweis, X., Gossart, A., et al.: What is the surface mass balance of Antarctica? An intercomparison of regional climate model estimates, The Cryosphere, 15, 3751–3784, 2021.

Mouginot, J., Rignot, E., and Scheuchl, B.: Sustained increase in ice discharge from the Amundsen Sea Embayment, West Antarctica, from 1973 to 2013, Geophysical Research Letters, 41, 1576–1584, 2014.

Müller, W. A., Jungclaus, J. H., Mauritsen, T., Baehr, J., Bittner, M., Budich, R., Bunzel, F., Esch, M., Ghosh, R., Haak, H., et al.: A higher-resolution version of the max planck institute earth system model (MPI-ESM1. 2-HR), Journal of Advances in Modeling Earth Systems, 10, 1383–1413, 2018.

Nakayama, Y., Menemenlis, D., Zhang, H., Schodlok, M., and Rignot, E.: Origin of Circumpolar Deep Water intruding onto the Amundsen and Bellingshausen Sea continental shelves, Nature communications, 9, 1–9, 2018.

Naughten, K. A., Meissner, K. J., Galton-Fenzi, B. K., England, M. H., Timmermann, R., and Hellmer, H. H.: Future projections of Antarctic ice shelf melting based on CMIP5 scenarios, Journal of Climate, 31, 5243–5261, 2018.

Naughten, K. A., Jenkins, A., Holland, P. R., Mugford, R. I., Nicholls, K. W., and Munday, D. R.: Modeling the Influence of the Weddell Polynya on the Filchner–Ronne Ice Shelf Cavity, Journal of Climate, 32, 5289–5303, 2019.

Naughten, K. A., De Rydt, J., Rosier, S. H., Jenkins, A., Holland, P. R., and Ridley, J. K.: Two-timescale response of a large Antarctic ice shelf to climate change, Nature communications, 12, 1–10, 2021.

Nias, I. J., Cornford, S. L., Edwards, T. L., Gourmelen, N., and Payne, A. J.: Assessing uncertainty in the dynamical ice response to ocean warming in the Amundsen Sea Embayment, West Antarctica, Geophysical Research Letters, 46, 11 253–11 260, 2019.

Nowicki, S., Goelzer, H., Seroussi, H., Payne, A. J., Lipscomb, W. H., Abe-Ouchi, A., Agosta, C., Alexander, P., Asay-Davis, X. S., Barthel, A., et al.: Experimental protocol for sea level projections from ISMIP6 stand-alone ice sheet models, The Cryosphere, 14, 2331–2368, 2020.

Paolo, F. S., Fricker, H. A., and Padman, L.: Volume loss from Antarctic ice shelves is accelerating, Science, 348, 327–331, 2015.

Pattyn, F.: The paradigm shift in Antarctic ice sheet modelling, Nature communications, 9, 2728, 2018.

Pattyn, F. and Morlighem, M.: The uncertain future of the Antarctic Ice Sheet, Science, 367, 1331–1335, 2020.

Purich, A. and England, M. H.: Historical and future projected warming of Antarctic Shelf Bottom Water in CMIP6 models, Geophysical Research Letters, 48, e2021GL092 752, 2021.

Rignot, E., Mouginot, J., and Scheuchl, B.: Ice flow of the Antarctic ice sheet, Science, 333, 1427–1430, 2011.

Rignot, E., Jacobs, S., Mouginot, J., and Scheuchl, B.: Ice-shelf melting around Antarctica, Science, 341, 266–270, 2013.

Rignot, E., Mouginot, J., Scheuchl, B., Van Den Broeke, M., Van Wessem, M. J., and Morlighem, M.: Four decades of Antarctic Ice Sheet mass balance from 1979–2017, Proceedings of the National Academy of Sciences, 116, 1095–1103, 2019.

Robel, A. A., Seroussi, H., and Roe, G. H.: Marine ice sheet instability amplifies and skews uncertainty in projections of future sea-level rise, Proceedings of the National Academy of Sciences, 116, 14 887–14 892, 2019.

750 Rosier, S. H., Reese, R., Donges, J. F., De Rydt, J., Gudmundsson, G. H., and Winkelmann, R.: The tipping points and early warning indicators for Pine Island Glacier, West Antarctica, The Cryosphere, 15, 1501–1516, 2021.

Schoof, C.: The effect of cavitation on glacier sliding, Proceedings of the Royal Society A: Mathematical, Physical and Engineering Sciences, 461, 609–627, 2005.

Schoof, C.: Marine ice-sheet dynamics. Part 1. The case of rapid sliding, Journal of Fluid Mechanics, 573, 27–55, 2007.

755 Séférian, R., Nabat, P., Michou, M., Saint-Martin, D., Voldoire, A., Colin, J., Decharme, B., Delire, C., Berthet, S., Chevallier, M., et al.: Evaluation of CNRM earth system model, CNRM-ESM2-1: Role of earth system processes in present-day and future climate, Journal of Advances in Modeling Earth Systems, 11, 4182–4227, 2019.

Seroussi, H., Nowicki, S., Simon, E., Abe-Ouchi, A., Albrecht, T., Brondex, J., Cornford, S., Dumas, C., Gillet-Chaulet, F., Goelzer, H., et al.: initMIP-Antarctica: an ice sheet model initialization experiment of ISMIP6, The Cryosphere, 13, 1441–1471, 2019.

760 Seroussi, H., Nowicki, S., Payne, A. J., Goelzer, H., Lipscomb, W. H., Abe Ouchi, A., Agosta, C., Albrecht, T., Asay-Davis, X., Barthel, A., Calov, R., Cullather, R., Dumas, C., Gladstone, R., Golledge, N., Gregory, J. M., Greve, R., Hatterman, T., Hoffman, M. J., Humbert, A., Huybrechts, P., Jourdain, N. C., Kleiner, T., Larour, E., Leguy, G. R., Lowry, D. P., Little, C. M., Morlighem, M., Pattyn, F., Pelle, T., Price, S. F., Quiquet, A., Reese, R., Schlegel, N.-J., Shepherd, A., Simon, E., Smith, R. S., Straneo, F., Sun, S., Trusel, L. D., Van Breedam, J., van de Wal, R. S. W., Winkelmann, R., Zhao, C., Zhang, T., and Zwinger, T.: ISMIP6 Antarctica: a multi-model ensemble of the
765 Antarctic ice sheet evolution over the 21st century, The Cryosphere Discussions, 2020, 1–54, https://doi.org/10.5194/tc-2019-324, https://www.the-cryosphere-discuss.net/tc-2019-324/, 2020.

Shapiro, N. and Ritzwoller, M.: Inferring surface heat flux distributions guided by a global seismic model: particular application to Antarctica, Earth Planet. Sci. Lett., 223, 213–224, https://doi.org/10.1016/j.epsl.2004.04.011, 2004.

Siahaan, A., Smith, R., Holland, P., Jenkins, A., Gregory, J. M., Lee, V., Mathiot, P., Payne, T., Ridley, J., and Jones, C.: The Antarctic contri-
770 bution to 21st century sea-level rise predicted by the UK Earth System Model with an interactive ice sheet, The Cryosphere Discussions, pp. 1–42, 2021.

Snow, K., Goldberg, D., Holland, P. R., Jordan, J. R., Arthern, R. J., and Jenkins, A.: The response of ice sheets to climate variability, Geophysical Research Letters, 44, 11–878, 2017.

Still, H., Campbell, A., and Hulbe, C.: Mechanical analysis of pinning points in the Ross Ice Shelf, Antarctica, Annals of Glaciology, 60,
775 32–41, 2019.

Sun, S., Pattyn, F., Simon, E. G., Albrecht, T., Cornford, S., Calov, R., Dumas, C., Gillet-Chaulet, F., Goelzer, H., Golledge, N. R., et al.: Antarctic ice sheet response to sudden and sustained ice-shelf collapse (ABUMIP), Journal of Glaciology, 66, 891–904, 2020.

Swart, N. C., Cole, J. N., Kharin, V. V., Lazare, M., Scinocca, J. F., Gillett, N. P., Anstey, J., Arora, V., Christian, J. R., Hanna, S., et al.: The Canadian earth system model version 5 (CanESM5. 0.3), Geoscientific Model Development, 12, 4823–4873, 2019.

780 van Wessem, J. M., Jan Van De Berg, W., Noël, B. P., Van Meijgaard, E., Amory, C., Birnbaum, G., Jakobs, C. L., Krüger, K., Lenaerts, J., Lhermitte, S., et al.: Modelling the climate and surface mass balance of polar ice sheets using RACMO2: Part 2: Antarctica (1979-2016), Cryosphere, 12, 1479–1498, 2018.

Voldoire, A., Saint-Martin, D., Sénési, S., Decharme, B., Alias, A., Chevallier, M., Colin, J., Guérémy, J.-F., Michou, M., Moine, M.-P., et al.: Evaluation of CMIP6 deck experiments with CNRM-CM6-1, Journal of Advances in Modeling Earth Systems, 11, 2177–2213, 2019.

785 Waibel, M., Hulbe, C., Jackson, C., and Martin, D.: Rate of mass loss across the instability threshold for Thwaites Glacier determines rate of mass loss for entire basin, Geophysical Research Letters, 45, 809–816, 2018.

Weertman, J.: Stability of the junction of an ice sheet and an ice shelf, Journal of Glaciology, 13, 3–11, 1974.

Wu, T., Lu, Y., Fang, Y., Xin, X., Li, L., Li, W., Jie, W., Zhang, J., Liu, Y., Zhang, L., et al.: The Beijing Climate Center climate system model (BCC-CSM): the main progress from CMIP5 to CMIP6, Geoscientific Model Development, 12, 1573–1600, 2019.

790 Wyser, K., Kjellström, E., Koenigk, T., Martins, H., and Döscher, R.: Warmer climate projections in EC-Earth3-Veg: the role of changes in the greenhouse gas concentrations from CMIP5 to CMIP6, Environmental Research Letters, 15, 054 020, 2020.

Xin-Yao, R., Jian, L., Hao-Ming, C., Yu-Fei, X., Jing-Zhi, S., Li-Juan, H., et al.: Introduction of CAMS-CSM model and its participation in CMIP6, Advances in Climate Change Research, 15, 540, 2019.

Zoet, L. K. and Iverson, N. R.: A slip law for glaciers on deformable beds, Science, 368, 76–78, 2020.